



**HAL**  
open science

# Study of asymmetrically heated flows passing through gas-pressurized solar receivers using Direct Numerical Simulations

Martin David, Adrien Toutant, Françoise Bataille

► **To cite this version:**

Martin David, Adrien Toutant, Françoise Bataille. Study of asymmetrically heated flows passing through gas-pressurized solar receivers using Direct Numerical Simulations. *International Journal of Heat and Mass Transfer*, 2023, 201, pp.123577. 10.1016/j.ijheatmasstransfer.2022.123577 . hal-04002561

**HAL Id: hal-04002561**

**<https://hal.science/hal-04002561>**

Submitted on 23 Feb 2023

**HAL** is a multi-disciplinary open access archive for the deposit and dissemination of scientific research documents, whether they are published or not. The documents may come from teaching and research institutions in France or abroad, or from public or private research centers.

L'archive ouverte pluridisciplinaire **HAL**, est destinée au dépôt et à la diffusion de documents scientifiques de niveau recherche, publiés ou non, émanant des établissements d'enseignement et de recherche français ou étrangers, des laboratoires publics ou privés.

## Highlights

### **Study of asymmetrically heated flows passing through gas-pressurized solar receivers using Direct Numerical Simulations**

Martin David, Adrien Toutant, Françoise Bataille

- DNS of highly anisothermal and turbulent channel flows are performed and analyzed.
- Integral values, turbulence statistics, PDF, and spectra are investigated.
- Differences and similarities between wall heat flux and wall friction are highlighted.
- PDF of wall heat flux and wall friction are well fitted with skewed Gaussian models.
- Ratio between wall heat flux and wall friction is linked to turbulent structure size.

# Study of asymmetrically heated flows passing through gas-pressurized solar receivers using Direct Numerical Simulations

Martin David<sup>a</sup>, Adrien Toutant<sup>a,\*</sup> and Françoise Bataille<sup>a</sup>

<sup>a</sup>Laboratoire PROMES-CNRS (UPR 8521), Université de Perpignan via Domitia, Technosud-Rambla de la thermodynamique, Perpignan, 66100, France

---

## ARTICLE INFO

### Keywords:

Direct Numerical Simulation  
High wall heat fluxes  
High temperatures  
Asymmetrical heating  
Wall friction  
Turbulence  
Solar receiver

## ABSTRACT

Solar receiver flows are very complex since the heating fluid is strongly turbulent and asymmetrically heated at high temperature levels. To deepen the understanding of these flows, four DNS have been performed in different fluid heating configurations. The Navier-Stokes and the energy equations are solved under the low Mach approximation and the coupling between the dynamics and the temperature is taken into account. A simplified geometry of solar receiver is used and consists in a bi-periodical channel flow with fixed wall temperatures. The hot and cold wall temperatures are respectively 1300K and 900K and the mean friction Reynolds number is 820. Integral, mean and fluctuating quantities are investigated. Afterwards, quantitative and qualitative studies of instantaneous fields of wall heat flux and wall friction are carried out. In particular, probability density functions and 1D spectral analyses are discussed. This work highlights the strong coupling between the dynamics and the temperature. Focusing on wall heat fluxes, it seems that the ratio between the fluctuations and the mean quantity is weakly dependent of the studied conditions and is about 0.44 at both walls in all the simulations. The wall heat flux and the wall friction are highly correlated. The probability density functions indicate that the most probable wall heat fluxes, respectively wall frictions, are below the mean wall heat flux, respectively wall friction. They can be well approximated with skewed Gaussian distributions. The turbulent structures associated with wavenumbers lying between  $k_x^+ = 0.03$  and  $k_x^+ = 0.05$  and those associated to small wavenumbers in the spanwise direction seems to favor the heat transfer while keeping a wall friction relatively low.

---

## 1. Introduction


The Concentrated Solar Power (CSP) generation was about 14.5 TWh in 2020. In the Net Zero Scenario proposed by the International Energy Agency (IEA), the power generated by this technology should reach 204.0 TWh in 2030 (IEA co, 2021). To achieve this objective, the annual average growth should be almost 31%. The global cost fell by 68% between 2010 and 2020. This is mainly due to a 50% reduction in the global weighted-average total installed costs of newly commissioned CSP plants, a 41% gain in capacity factors thanks to the use of heat storage systems, and a 33% decrease in operation and maintenance costs. According to IRENA report (IRENA co, 2021), the Levelized Cost of Energy (LCOE) of the solar tower was lying between 0.07 €/kWh and 0.2 €/kWh in 2018-2019. The optimization of the different parts of the system will help pursue the decline of the CSP LCOE.

A large number of studies are investigating new working fluids to permit the increase of the temperature

levels which enhance the system performances of solar tower power (Buck and Giuliano, 2019; Zheng et al., 2020; Merchán et al., 2022). Using air, there is no more limiting temperature due to the operating fluid, the maximum is then fixed with the resistance of the materials (Kribus et al., 1999). For that reason, extremely high temperatures can be reached. The new working fluids pave the way to research studies on heat transfer enhancement in solar receivers that are characterized by strong asymmetrical heating of the fluid. The encountered flows are very complex, that is why upstream works are necessary to deepen the understanding of the coupling between the dynamics and the temperature effects.

Direct Numerical Simulations (DNS) are commonly used to investigate flow physics in academic configurations. Channel flows are studied because this geometry is widely encountered in industry, particularly for heat exchangers in nuclear power plants, electronic devices, and solar receivers. In those applications, the flow is often turbulent and heated from the walls of the channel. If the temperature difference is small, the temperature effects on the fluid physical properties can be neglected and the momentum balance is often decoupled from the thermal energy balance. In the literature, most of the non-isothermal DNS are performed considering the temperature as a passive scalar. Some of them are described in the rest of the paragraph.

\*Corresponding author

 [martin.david@promes.cnrs.fr](mailto:martin.david@promes.cnrs.fr) (M. David);  
[adrien.toutant@univ-perp.fr](mailto:adrien.toutant@univ-perp.fr) (A. Toutant);  
[francoise.bataille@univ-perp.fr](mailto:francoise.bataille@univ-perp.fr) (F. Bataille)

 <https://perso.univ-perp.fr/adrien.toutant/research.html>  
(A. Toutant)

ORCID(s): 0000-0001-5213-8712 (M. David);  
0000-0002-7156-1732 (A. Toutant)

The following works deal with the link between the dynamic of the flow and the behavior of a passive scalar. The transport of a scalar was investigated thanks to a DNS by Kim and Moin (Kim and Moin, 1989). They notice that the scalar fields are strongly linked to the streamwise velocity and that the scalar fluxes could be modeled similarly to the momentum fluxes. Lyons *et al.* (Lyons et al., 1991) studied passive heat transfer in a channel flow at a bulk Reynolds number of 2300. They found reasonably good agreements between the obtained mean temperature profile, eddy conductivity profile, and turbulent Prandtl number and experimental results. The authors notice that the dominant wall eddies, which have a spanwise scale of about 50 wall units, manage both the Reynolds stress production and turbulent heat transfer at the wall by moving hot and cold pockets of fluid to and from the wall. They also highlight that in the channel center, the fluctuating temperature production and dissipation are significant. Kasagi *et al.* (Kasagi et al., 1992) studied turbulent air flow in channel. Their results suggest that the temperature fluctuations are highly correlated with the streamwise velocity fluctuations, especially near the walls. Abe and Antonia (Abe and Antonia, 2019) examined the turbulent Prandtl number for air and mercury in a turbulent channel flow under a constant time-averaged heat flux thermal boundary condition. They propose laws for estimating the turbulent Prandtl number in the different regions of the flow. Particularly, the authors highlight the fact that the decrease in turbulent Prandtl number in the region  $y/\delta > 0.2$  is due to the unmixedness of the scalar.

The influence of the Prandtl number is frequently investigated. Focusing on the budget of wall-normal heat flux, Kawamura *et al.* (Kawamura et al., 1998, 1999) notice that the temperature-pressure gradient correlation is prevailing as the destruction term for bigger Prandtl numbers while, for smaller Prandtl number, the dissipation term is. Na and Hanratty (Na et al., 1999) studied the effect of the Prandtl and the Schmidt numbers at a friction Reynolds number of 150. Their results show that the momentum and scalar transport analogy is not applicable to define the limiting behavior of turbulent diffusivity in the vicinity of the wall. Moreover, since the turbulent transport is weak in the conductive sublayer, this limiting relation cannot be used to calculate the concentration or temperature profile for large values of Prandtl or Schmidt numbers. The next studies are related to the influence of the Reynolds number. Three DNS at friction Reynolds number of 500, 1000 and 2000, with medium to low Prandtl number, were performed by Alcántara-Ávila *et al.* (Alcántara-Ávila et al., 2018). They notice that the logarithmic profile of the thermal flow appears for Prandtl number above 0.3 because of the thinner viscous thermal layer generated as the Prandtl number is increased. Alcántara-Ávila *et al.* (Alcántara-Ávila

and Hoyas, 2021) supplement the previous work with medium to high Prandtl number. They characterize the thermal field in those new conditions and notice that the near-wall maximum of temperature fluctuations is independent of the Reynolds number for sufficiently high Prandtl numbers, meaning above 7. DNS of turbulent heat transfer in a channel flow was carried out by Kozuka *et al.* (Kozuka et al., 2009). The results suggest that the wall-asymptotic value of the turbulent Prandtl number is almost independent of Reynolds number for the entire tested range of Prandtl number, meaning from 0.71 to 10. The turbulence level effect has been investigated by Abe *et al.* (Abe et al., 2004). The authors performed DNS at friction Reynolds numbers of 180, 395, 640 and 1020. They highlight that, for a Prandtl number of 0.71, the surface heat-flux fluctuations are very close to the streamwise wall shear-stress fluctuations, although differences are observed in the large positive and negative fluctuations. It appears that the large-scale structures seen in the surface heat-flux fluctuations are mostly phenomena linked to the large-scale motions for the thermal field of the outer layer.

In this paragraph, some works performed with temperature acting as an active scalar are presented. Aulery *et al.* (Aulery et al., 2017) carried out DNS at mean friction Reynolds of 180 and 395, with wall temperature of 293 K and 596 K. They establish the turbulent kinetic energy spectral equation and decompose them in three terms: production, nonlinear transfer and viscous effects. The authors discuss the influence of each terms in both isothermal and anisothermal conditions. It was pointed out that the purely anisothermal contribution transfers the energy from the hot side of the channel toward the cold side. This contribution is responsible for around 10% of the total process.

Avellaneda *et al.* (Avellaneda et al., 2019) discussed the local entropy generation rate thanks to DNS performed at mean friction Reynolds from 150 to 210, with wall temperature of 293 K and 879 K. The results suggest that an increase in the wall temperature ratio leads to larger entropy generation rates, and to accentuate the asymmetry between the cold wall and the hot wall. The authors notice that the entropy generation rates is always bigger at the cold wall than at the hot wall.

Orlandi *et al.* (Orlandi et al., 2016) investigated conjugate heat transfer in channel characterized by rough surfaces. Several type of roughness elements are analyzed. The sweeps and ejections events located in the near wall region are responsible for the modification of the flow structures, and thus the temperature distribution. It seems that the amplitude and the number of these events are highly correlated with the flow generated within the surfaces, and are affecting the temperature fluctuation profiles.



David *et al.* (David et al., 2021a) performed DNS of a highly turbulent channel flows under a strong asymmetric heating. This article was mainly dedicated to the study of Large-Eddy Simulations (LES), but a part deals with the investigation of the flow physics thank to two DNS. The results indicate that there is a strong coupling between the dynamic and the temperature. The wall-normal velocity is highly dependent of the temperature profile.

The presented state of the art shows that very few studies have been conducted in anisothermal conditions considering the temperature as an active scalar. Moreover, to the author's knowledge, the article of David *et al.* (David et al., 2021a) is the only paper handling the study of flow physics with DNS in the operating conditions of solar receiver, that are characterized by high Reynolds numbers, asymmetric heating of the fluid, and high wall heat fluxes. The present article aims to deepen the analyses presented in (David et al., 2021a) by investigating new temperature profiles, proposing new results, and using different scalings. A particular attention is paid to the similarities and differences between the wall heat flux and the wall friction.

The paper is organized as follows: Section 2 gives the resolved equations. The configurations studied are detailed in Section 3. The obtained DNS results are discussed in Section 4. Lastly, a final section concludes.

## 2. Low Mach number equations

In gas-pressurized solar receivers, the mass flow is high to improve the system performance but the flow is subsonic. Indeed, the Mach number is around 0.1. The thermal dilatation effects have to be considered but the influence of acoustic waves can be neglected. Thus, the Navier-Stokes equations are solved under the low Mach number approximation that is valid as long as the Mach number is below 0.3. This theory was proposed by Paolucci (Paolucci, 1982) and aims to narrow the gap between the incompressible and the compressible formulations of the Navier-Stokes equations. It permits suppressing the numerical constraints associated with the latter formulation. The resolved system is given by equations 1-4:

- Mass conservation equation

$$\frac{\partial \rho}{\partial t} + \frac{\partial \rho U_j}{\partial x_j} = 0, \quad (1)$$

- Momentum conservation equation

$$\frac{\partial \rho U_i}{\partial t} = -\frac{\partial \rho U_j U_i}{\partial x_j} - \frac{\partial P}{\partial x_i} + \frac{\partial \Sigma_{ij}}{\partial x_j}, \quad (2)$$

- Energy conservation equation

$$\frac{\partial U_j}{\partial x_j} = -\frac{1}{\gamma P_0} \left[ (\gamma - 1) \frac{\partial Q_j}{\partial x_j} + \frac{dP_0}{dt} \right], \quad (3)$$

- Ideal gas law

$$T = \frac{P_0}{\rho r}, \quad (4)$$

where  $\gamma$  is the heat capacity ratio. The pressure involved in the energy equation is the thermodynamical pressure, denoted  $P_0$ . It represents the mean pressure in the computational domain, and only depends on the time ( $\partial P_0 / \partial x_i = 0$ ). The mechanical pressure,  $P$ , appears in the momentum conservation equation and is spatially varying.

The particular form of the energy conservation equation which involves the velocity divergence is obtained (1) by applying the ideal gas law to the energy equation written in terms of transport of temperature; (2) by using the fact that the thermodynamical pressure is homogeneous. This formulation is also used by Nicoud (Nicoud, 2000) and Dupuy *et al.* (Dupuy et al., 2019).

The fluid is supposed to be Newtonian, leading to the following expression for the viscous stress tensor:

$$\Sigma_{ij}(U, T) = \mu(T) \left( \frac{\partial U_i}{\partial x_j} + \frac{\partial U_j}{\partial x_i} \right) - \frac{2}{3} \mu(T) \frac{\partial U_k}{\partial x_k} \delta_{ij}. \quad (5)$$

The conductive heat flux is given by the Fourier's law:

$$Q_j(T) = -\lambda(T) \frac{\partial T}{\partial x_j}, \quad (6)$$

where  $\mu(T)$  is the dynamic viscosity,  $\lambda(T)$  is the thermal conductivity, and  $\delta_{ij}$  the Kronecker symbol.

The fluid used is air. The viscosity is computed using the Sutherland's law (Sutherland, 1893):

$$\mu(T) = \mu_0 \frac{T^{3/2} T_0 + S}{T + S}, \quad (7)$$

where  $\mu_0 = 1.716 \times 10^{-5} \text{ Pa} \cdot \text{s}$ ,  $S = 110.4 \text{ K}$ , and  $T_0 = 273.15 \text{ K}$ . The Prandtl number is assumed to be constant so as the heat capacity at constant pressure which is computed with the average of the wall temperatures. The heat capacity is  $C_p = 1155 \text{ J} \cdot \text{kg}^{-1} \cdot \text{K}^{-1}$  for all the simulations. The Prandtl number depends on the simulations and is lying between 0.70 and 0.76. The conductivity is obtained from the Prandtl number, the heat capacity at constant pressure, and the viscosity:

$$\lambda(T) = \frac{C_p}{\text{Pr}} \mu(T). \quad (8)$$

The simulations are carried out with TrioCFD code (Calvin et al., 2002). To the best of the author's knowledge, there is no reference data in the working conditions of the gas-pressurized solar receiver produced by another research group. For that reason, the numerical method is validated by comparing the DNS results in the isothermal case with data from the literature. Dupuy *et al.* (Dupuy et al., 2018) already

performed validations at friction Reynolds numbers of 180 and 395 with reference DNS. David *et al.* (David *et al.*, 2021b) carried out a successful comparison with the DNS of Hoyas and Jimenez (Hoyas and Jiménez, 2008) at a friction Reynolds number of 930.

### 3. Flow analysis along a solar receiver

#### 3.1. Study configuration

The solar absorber is composed of an irradiated wall and an insulated wall. The first receives the concentrated solar radiation and transfers heat to the fluid by conduction and to the insulated wall by radiation. It results in fluid heating from both sides of the solar receiver. As the temperature is always higher at the irradiated wall than at the insulated wall, the flow is asymmetrically heated.

In these works, the flow passing through the solar receiver is modeled with an academic bi-periodical channel flow. The domain size is  $L_x = 4\pi\delta$ ,  $L_y = 2\delta$ , and  $L_z = 4/3\pi\delta$  with  $L_x$ ,  $L_y$ , and  $L_z$  the lengths in the streamwise, wall-normal, and spanwise directions, respectively. The half-channel height is denoted  $\delta$  and is 3 mm. See Figure 1 for a schematic view of the investigated channel flow. The simulations are per-

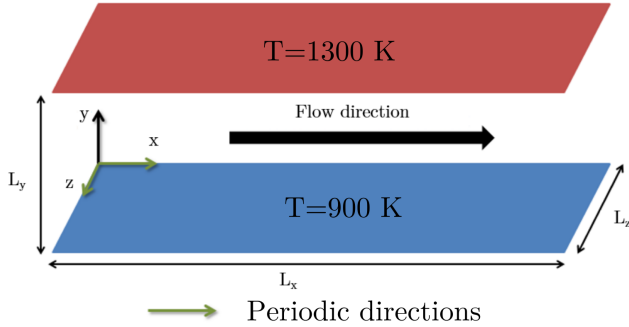


Figure 1: Investigated channel flow.

formed with a staggered grid system. Mesh is uniform in the homogeneous directions. It follows the hyperbolic tangent law described by Equation 9 in the wall-normal direction to capture the strong velocity and temperature gradients induced by the walls.

$$y_k = L_y \left( 1 + \frac{1}{a} \tanh \left[ \left( \frac{k-1}{N_y-1} \right) \tanh^{-1}(a) \right] \right) \quad (9)$$

where  $a$  is the mesh dilatation parameter and  $N_y$  is the number of grid points in the wall-normal direction. The mesh consists in 660 millions of cells that are distributed as follows:  $N_x \times N_y \times N_z = 1152 \times 746 \times 768$ . The normalized cell sizes of the used mesh are:  $\Delta x^+ = 10.9$ ,  $\Delta y^+(0) = 0.42$ ,  $\Delta y^+(\delta) = 5.4$ ,  $\Delta z^+ = 5.4$ . These values are given for the cold side of the channel which correspond to the highest friction Reynolds number. Notice that for the simulation associated with the smallest Kolmogorov length scale gives  $\eta = \left( \frac{\nu^3}{\epsilon} \right)^{1/4} \approx$

$1.5 \times 10^{-6}$  meter. The first cell size in the wall-normal direction is slightly lower, with a length of  $1.3 \times 10^{-6}$  meter, which is in agreement with the classical DNS requirement (Kim *et al.*, 1987). The Batchelor scale gives the smallest length scales of fluctuations in scalar concentration that can exist before molecular diffusion prevail. The smallest length scale is computed with the thermal diffusivity at the cold wall and is  $9.7 \times 10^{-6}$  meter which is 7.5 times bigger than the size of the first cell in the wall direction.

The channel consists of fixed wall temperatures to simulate several sections of the solar absorber. The streamwise and spanwise directions are periodic which allows the convergence of the flow statistics but forces the study of a fully developed flow. A source term is then introduced in the energy equation to compensate for the contributions of the walls. Modifying the heat sink permits studying various temperature profiles, *i.e.* various axial locations in the solar receiver. The energy equation described by equation (3) becomes:

$$\frac{\partial U_j}{\partial x_j} = -\frac{1}{\gamma P_0} \left[ (\gamma - 1) \left( \frac{\partial Q_j}{\partial x_j} - H_s \right) + \frac{dP_0}{dt} \right], \quad (10)$$

where  $H_s$  is the volumic heat sink.

#### 3.2. Investigated conditions

In concentrated solar systems, the fluid enters the solar receiver at a relatively low temperature and is heated by the walls. The gap between the bulk temperature and the wall temperature becomes smaller as the fluid progresses in the absorber (Capeillère *et al.*, 2014). To deepen the understanding of the coupling between the dynamics and the temperature, four anisothermal flow configurations are investigated. In addition, a DNS in isothermal conditions is studied to highlight the temperature effects of the anisothermal simulations. For the anisothermal simulations, the wall temperatures are fixed to 900 K and 1300 K to be representative of the temperature levels reached by the irradiated and insulated walls of the solar receivers. The heat sink values are chosen to obtain several fluid temperature that are encountered in the operating conditions of solar receivers. The heat sink permits investigating flows of various axial locations in the solar receiver. The higher the heat sink, the higher temperature gap between the fluid and the walls and thus the closer from the inlet of the solar absorber. These five DNS are listed in Table 1. The mean friction Reynolds number is defined as the average of the hot and cold friction Reynolds number given by  $Re_{\tau,w} = U_{\tau,w} \delta / \nu_w$ , where the subscript  $w$  denotes the values computed at the wall and  $U_{\tau,w}$  is the friction velocity. For all the simulations carried out in anisothermal conditions, the mean friction Reynolds number is imposed and is about 820. Since the wall temperatures are different and the fluid properties depend on the temperature, the cold, respectively hot, friction Reynolds number

Simulation	$T_w^h - T_w^c$ [K]	$H_s$ [MW/m <sup>3</sup> ]	$T_b$ [K]
isoT-S0	293 - 293	0	293
anisoT-S0	1300 - 900	0	1093
anisoT-S1	1300 - 900	55	883
anisoT-S2	1300 - 900	109	690
anisoT-S3	1300 - 900	164	525

Table 1: Investigated thermal conditions.

is about 1000, respectively 640. Hence, the turbulence level is higher on the cold side than on the hot side. The isothermal DNS has been performed at a friction Reynolds number of 930 for the code validation with the reference DNS of Hoyas and Jiménez (Hoyas and Jiménez, 2008). Both simulations are in very good agreement. See David *et al.* (David et al., 2021a) for the comparison between the two DNS. The skin friction coefficient obtained with the isothermal DNS performed in this study is  $C_f = 4.95 \times 10^{-3}$ . This is in good agreement with the skin friction coefficient obtained by Hoyas and Jimenez (Hoyas and Jiménez, 2008) since the relative error is inferior to 1.1%. The thermodynamical pressure is set to 10 bar in all the simulations. Note that the simulated times of the DNS are about 45 characteristic times, computed at the cold wall with  $(\delta/U_{\tau,c})$ . The data collection duration is 20 characteristic times.

## 4. Results and discussion

In this section, the results of the five DNS are presented and discussed. Integral quantities as well as first- and second-order statistics of turbulence are investigated then the focus is placed on the study of differences and similarities between wall heat flux and wall friction.

The symbol ".+" indicates that the results are normalized in wall units:  $x_i^+ = x_i U_{\tau,w} / \nu_w$ ,  $U_i^+ = U_i / U_{\tau,w}$ ,  $T^+ = (T_w - T) / T_{\tau,w}$ , and  $\langle u'_i u'_j \rangle^+ = \langle u'_i u'_j \rangle / U_{\tau,w}^2$ . The friction velocity and the friction temperature are respectively expressed as  $U_{\tau,w} = \sqrt{\nu_w \partial U_1 / \partial x_2}$ , and  $T_{\tau,w} = \phi_w / (\rho_w C_p U_{\tau,w})$ , with  $\phi_w$  the conductive heat flux at the wall. The symbol  $U_i$  denotes the  $i$ th component of velocity, and  $x_i$  denote the Cartesian coordinate in the  $i$ th direction. To shorten the notations, the subscript is sometimes removed. In this case  $U$  accounts for  $U_1$ . The symbols  $\nu_w$ ,  $\mu_w$ , and  $\rho_w$  respectively account for the kinematic viscosity, the dynamic viscosity, and the density at walls. Note that since there are two different wall temperatures, the quantities followed by the subscript "w" can take two values: either the value associated with the hot wall and the value associated with the cold wall.

The Van Driest scaling (Driest, 1956) is employed for the streamwise velocity. It is given by:

$$U_{VD}^+ = \frac{2}{Pr_t T_{\tau,w} / T_w} \left( 1 - \sqrt{1 - Pr_t T_{\tau,w} / T_w U / U_{\tau,w}} \right). \quad (11)$$

Note that the values used for the turbulent Prandtl number are those obtained by averaging wall-normal profiles for each simulation.

The symbol ".\*" indicates that the results are normalized with the semi-local scaling (Patel et al., 2015; Trettel and Larsson, 2016) that takes into account the local variations of density and kinematic viscosity:  $x_i^* = x_i U_{\tau,w}^* / \nu(y)$ ,  $U_i^* = U_i / U_{\tau,w}^*$ ,  $T^+ = (T_w - T) / T_{\tau,w}^*$ , and  $\langle u'_i u'_j \rangle^* = \langle u'_i u'_j \rangle / U_{\tau,w}^{*2}$ . The friction velocity and the friction temperature are respectively expressed as  $U_{\tau,w}^* = \sqrt{\mu_w / \rho(y) \partial U_1 / \partial x_2}$ , and  $T_{\tau,w}^* = \phi_w / (\rho(y) C_p U_{\tau,w}^*)$ . Note that, the semi-local scaling computes the wall friction with the wall viscosity but the quantities are expressed locally. The wall friction velocity is influenced by the local variations of the density.

The symbol ".o" signifies that the flow parameters are normalized with the mean friction velocity or temperature:  $U_i^o = U_i / U_{\tau,w}^{mean}$ ,  $T^o = (T_w - T) / T_{\tau,w}^{mean}$ . The velocity - temperature and temperature - temperature are similarly scaled  $\langle u'_i \theta' \rangle^o = \langle u'_i \theta' \rangle / (U_{\tau,w}^{mean} T_{\tau,w}^{mean})$  and  $\langle \theta' \theta' \rangle^o = \langle \theta' \theta' \rangle / (T_{\tau,w}^{mean2})$ . Here, the notation *.mean* denote the averaging of the values obtained at both walls. This scaling is well adapted to discuss the quantity variations along the entire channel height.

### 4.1. Integral quantities

Integral quantities permit rapidly characterizing the flow. They are frequently used in the literature and can be approximated with correlations. In this subsection, the integral quantities related to the dynamic of the flow are firstly given and discussed, then the wall heat fluxes are discussed.

Table 2 provides information on integral quantities associated with the flow dynamics. The results show that for a given mean wall friction, the higher the heat sink, the higher the mass flow. When the fluid temperature decreases, the velocity profile is rather flattened. Indeed, the ratio  $U_c / U_b$  diminishes from 1.135 in the "anisoT-S0" DNS to 1.117 in the "anisoT-S3" DNS. The cold wall skin friction coefficient is higher than the hot wall one. The lowest skin friction coefficients are obtained with the simulations performed with the highest heat sinks despite the mass flow increases. This is due to the reduction of the bulk velocity observed in these DNS. The Dean correlation (Dean, 1978) gives a good approximation of the skin friction coefficient in the isothermal case ( $\epsilon=5.8\%$ ) considering the bulk Reynolds number computed with a characteristic length of  $2\delta$ . In the anisothermal case, the wall skin

Simulation	Mass flow [kg/s]	$U_c/U_b$	$Re_b$	$C_f^h$	$C_f^c$	$C_f^{mean}$		
						DNS	Corr	$\epsilon$
isoT-S0	$8.50 \times 10^{-3}$	1.135	37392	$4.95 \times 10^{-3}$	$4.95 \times 10^{-3}$	$4.95 \times 10^{-3}$	$5.25 \times 10^{-3}$	5.8%
anisoT-S0	$1.64 \times 10^{-2}$	1.135	29988	$5.08 \times 10^{-3}$	$5.47 \times 10^{-3}$	$5.28 \times 10^{-3}$	$5.55 \times 10^{-3}$	4.9%
anisoT-S1	$1.98 \times 10^{-2}$	1.131	40928	$4.85 \times 10^{-3}$	$5.33 \times 10^{-3}$	$5.09 \times 10^{-3}$	$5.13 \times 10^{-3}$	0.8%
anisoT-S2	$2.44 \times 10^{-2}$	1.127	59222	$4.39 \times 10^{-3}$	$4.89 \times 10^{-3}$	$4.64 \times 10^{-3}$	$4.68 \times 10^{-3}$	0.9%
anisoT-S3	$2.99 \times 10^{-2}$	1.117	85568	$3.68 \times 10^{-3}$	$4.17 \times 10^{-3}$	$3.92 \times 10^{-3}$	$4.27 \times 10^{-3}$	8.1%

Table 2: Flow mean quantities relative to the dynamic. The skin friction coefficient obtained with the Dean correlation (Dean, 1978) are indicated with the word "Corr" and are compared with the DNS results. The superscript *mean* indicates that the hot and cold values are averaged. Note that the definition of the mean skin friction as the mean value of the hot and cold wall value is equivalent to the definition of the skin friction which is defined by the wall-shear stress that balances the pressure gradient in the flow system.

frictions are computed at both walls then an average is performed. The correlation permits estimating the average of the wall skin friction coefficients with 8.1% of error at most.

Table 3 provides information relative to the wall heat fluxes. The results point out that the simulation "anisoT-S0" has the same conductive wall heat fluxes at both walls. This was expected since the flow is periodic and fully developed. When the heat sink is involved, the wall heat fluxes are no more identical for a given simulation. The maximum asymmetry between the two walls is obtained for the simulation "anisoT-S1" ( $|\phi^h/\phi^c| = 4.1$ ). The highest heat flux is obtained at the hot wall of the simulation "anisoT-S3". The Nusselt number is a widely used dimensionless number in the turbulent heat and mass transfer between a fluid and a solid wall. The heat transfer correlation of David *et al.* (David et al., 2021c) dedicated to asymmetrical heating conditions is assessed with carried out DNS. The correlation gives very good estimations of the wall heat fluxes with a maximum relative error of 4.1%.

## 4.2. First-order statistics

In this subsection, first-order statistics are investigated. Figure 2 plots the profiles of  $\cdot^o$  scaled streamwise velocity, wall-normal velocity, and temperature as functions of the channel height. Focusing on the top-left graph, the results of anisothermal simulations show that the streamwise velocity decreases as the heat sink grows. To maintain a constant mean wall friction, the streamwise velocity has to be reduced when the fluid temperature drop. The normalized velocity is higher in the isothermal case than in anisothermal configurations due to the scaling with the mean friction velocity. The maximum streamwise velocity is slightly shifted toward the hot side of the channel due to fluid property variations. The wall-normal velocity is induced by temperature variations. Indeed, it is null in the isothermal case and the peak amplitude grows with the increase of the gap between the bulk temperature and the wall temperature. In the case

without a heat sink (anisoT-S0), the profile exhibits a "u" shape because the temperature gradient induces a wall-normal velocity flux from the hot wall to the cold wall. For the other DNS, the fluid is heated from both walls. Thermal expansion forces it to move away from the walls, which leads to wall-normal velocities oriented toward the channel center line. The peaks are opposed (positive on the hot side and negative on the cold side) and their amplitudes are higher on the hot side than on the cold side due to the bigger hot wall heat flux. The peaks are localized in the log-layer at  $y/(2\delta) \approx 0.022$  corresponding to a distance from the wall of  $y^+ \approx 45$ . The higher the asymmetry of the temperature gradient between the two walls is, the closer to the cold wall the wall-normal velocity crosses the zero line: around  $y/(2\delta) = 0.2$  for the simulation "anisoT-S1" whereas it appears around  $y/(2\delta) = 0.4$  for the simulation "anisoT-S3". The normalized wall-normal velocity is equal to  $-0.007$  in wall unit for all the simulations at the normalized distance  $y/(2\delta) = 0.48$ . For the DNS performed without a heat sink, the temperature profile indicates that the fluid temperature is equal to the average of the wall temperature at the location  $y/(2\delta) = 0.53$ , meaning on the hot side. For the other DNS, the weaker the heat sink, the closer to the cold wall the minimum temperature. Indeed, for the simulation "anisoT-S1", "anisoT-S2", and "anisoT-S3" the minimum of temperature are respectively obtained for  $y/(2\delta) = 0.21, 0.35$  and  $0.40$ .

Figure 3 shows the profiles of density and kinematic viscosity as functions of the normalized channel height. The density linked to the temperature by the expression  $\rho \propto 1/T$  because of the use of the ideal gas law and the low Mach Mach number approximation. For that reason, the density profile presents reverse tendencies when compared to the temperature profile. The kinematic viscosity is defined with the density and the dynamic viscosity, which is linked to the temperature by the Sutherland's law, see Eq. 7. The same behaviors are observed for the temperature and the viscosity profiles. When the heat sink grows, the fluid temperature is

Simulation	$\phi^h$	$\phi^c$	$ \phi^h/\phi^c $	$Nu^h$			$Nu^c$		
	[kW/m <sup>2</sup> ]	[kW/m <sup>2</sup> ]		DNS	Corr	$\epsilon$	DNS	Corr	$\epsilon$
anisoT-S0	98.4	98.4	1.0	88.6	87.2	-1.6%	117.7	nr	-
anisoT-S1	262.5	-63.7	4.1	117.1	112.3	-4.1%	876.5	nr	-
anisoT-S2	441.0	-244.4	1.8	134.4	132.8	-1.2%	269.0	272.0	1.1%
anisoT-S3	587.1	-410.2	1.4	140.9	146.5	4.0%	253.2	245.0	-3.3%

Table 3: Mean flow quantities relative to temperature effects. "nr" signifies non relevant and corresponds to operating conditions that are beyond the applicability domain of the correlation of David *et al.* (David *et al.*, 2021c). The correlation results are associated with the word "Corr".

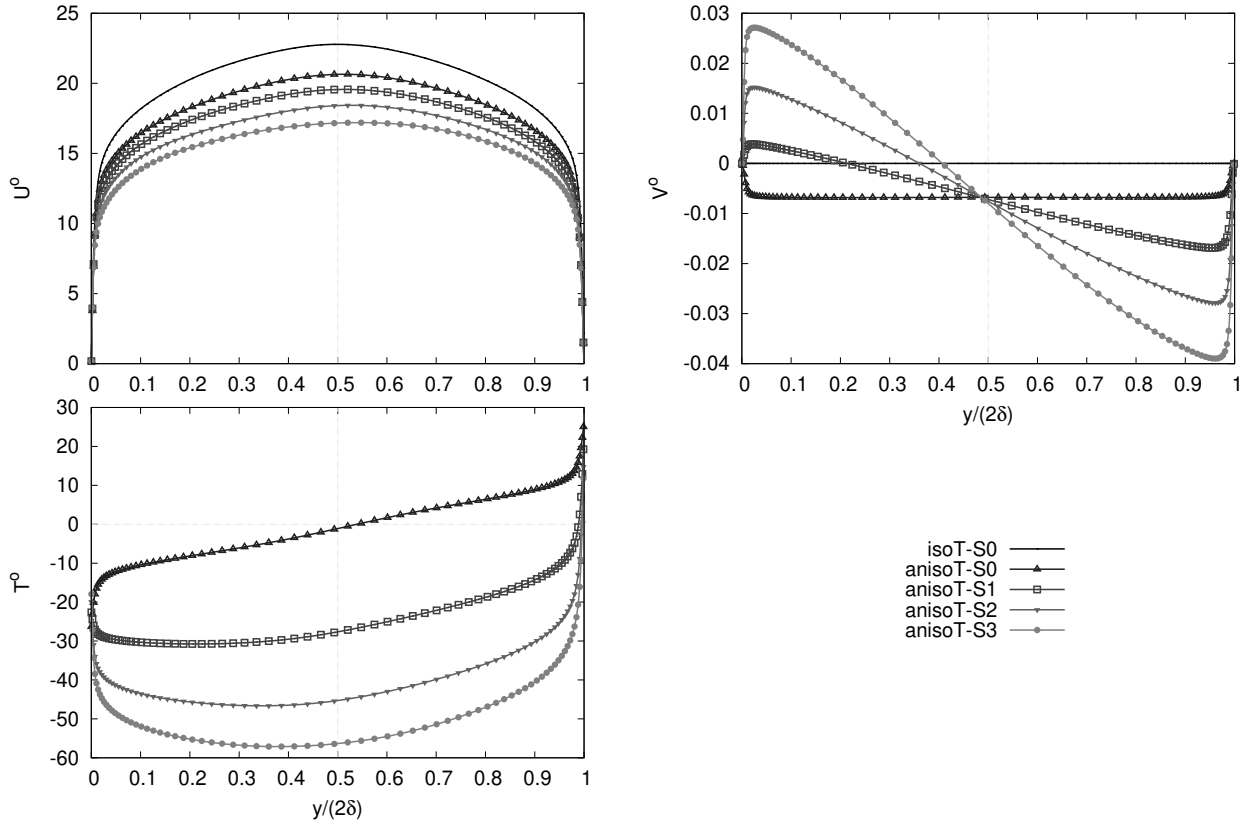


Figure 2: Profiles of scaled streamwise velocity, wall-normal velocity, and temperature as functions of the normalized channel height.

reduced which induces a reduction of the kinematic viscosity.

The profiles of wall scaled streamwise velocity and temperature are plotted in Figure 4. For both quantities, the curves overlap until  $y^+ = 10$ , then significant discrepancies arise. With this scaling, the streamwise profiles have the almost the same slope in the region  $50 < y^+ < 300$  but different offsets. For the temperature profile, the same observations can be made but in the range  $50 < y^+ < 100$ . The cold side profiles are higher than the hot side ones. In this region, the simulations performed with the highest wall heat fluxes are characterized by the lowest profiles and the gap

between the two sides of a given simulation decreases with the increase of the Reynolds number. The higher the wall heat fluxes, the more significant the distance between the law of the wall and the velocity profiles. In the isothermal case, the wall functions give a good approximation of the streamwise velocity profile in the range  $y^* < 5$  for  $f_1$  and  $30 < y^* < 400$  for  $f_2$ . They are defined by:

$$f_1(y^*) = y^*, \quad (12)$$

and

$$f_2(y^*) = \frac{1}{\kappa} \ln(y^*) + C, \quad (13)$$

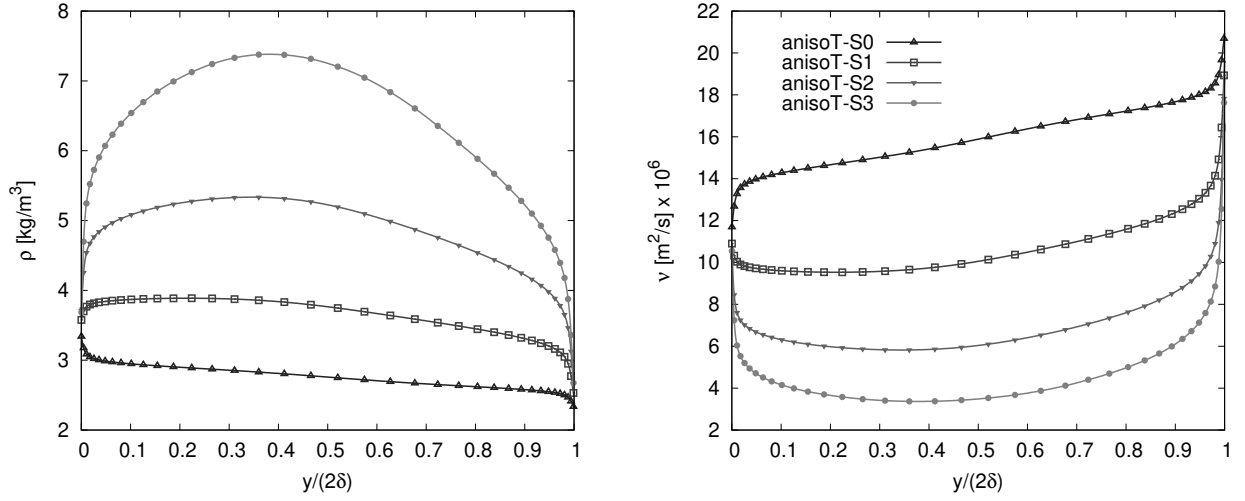


Figure 3: Profiles of density and kinematic viscosity as functions of the normalized channel height.

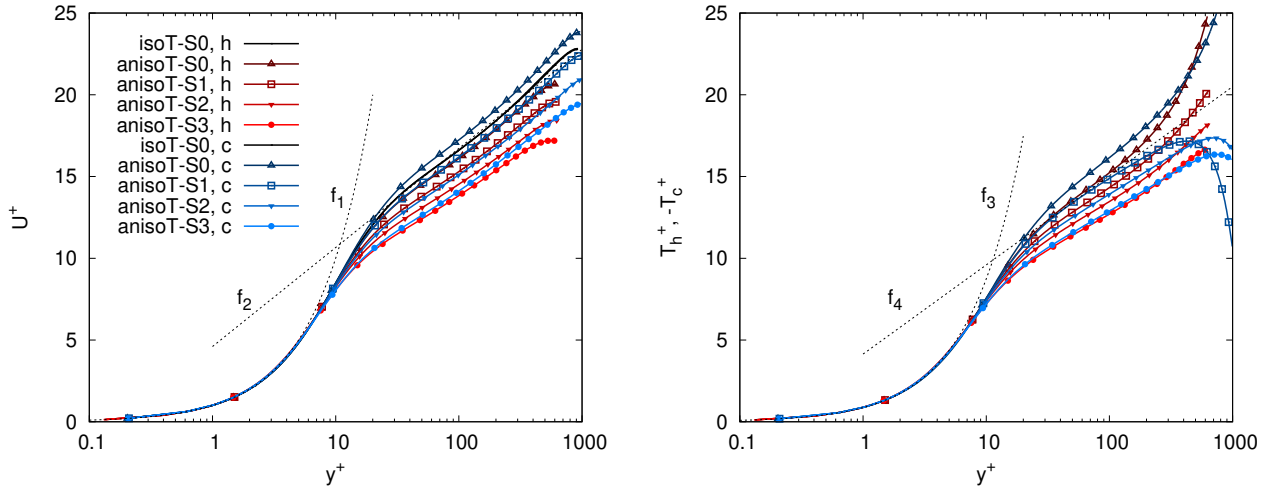


Figure 4: Profiles of wall scaled streamwise velocity and temperature as functions of the normalized channel height.

with  $\kappa = 0.38$  and  $C = 4.6$ .

The wall functions associated with the temperature profiles are given for information, they are discussed with the semi-local scaling in Figure 5.

The first-order statistics normalized with the semi-local scaling are presented in Figure 5. This normalization permits analyzing the results without the mean density and viscosity influence. The streamwise velocity profiles are very close then they split up after  $y^* = 10$ , as noticed in (Bellec et al., 2017). Increasing the heat sink results in increasing the normalized streamwise velocity in the center of the channel. The profile asymmetry is highlighted with the scaling. The streamwise velocity on the hot side is higher than the cold side one. The slope of the logarithmic law exhibits a downward trend with lowering wall heat flux. The profiles can be quite well approximated with the laws of the wall in the regions  $y^* < 5$  for  $f_1$  and  $30 < y^* < 400$  for  $f_2$ . Nevertheless, the results show that there are combined

effects of the wall-normal velocity and the turbulence level that affects the streamwise velocity. Indeed, the profile slopes in the logarithmic and outer regions are modified when compared to the isothermal case. The same tendencies and behaviors are observed for the temperature profiles. The curves associated with the lowest heat fluxes are quite well approached with the following laws of the wall:

$$f_3(y^*) = Pr y^* \text{ for } y^* < 5, \quad (14)$$

and

$$f_4(y^*) = Pr_t \left( \frac{1}{\kappa} \ln(y^*) + C \right) \text{ for } 30 < y^* < 200. \quad (15)$$

Figure 6 presents the streamwise velocity scaled with the Van Driest transformation as well as wall-normal velocity normalized with the wall scaling. The Van Driest scaling permits almost merging the streamwise velocity profiles. The slopes in the logarithmic

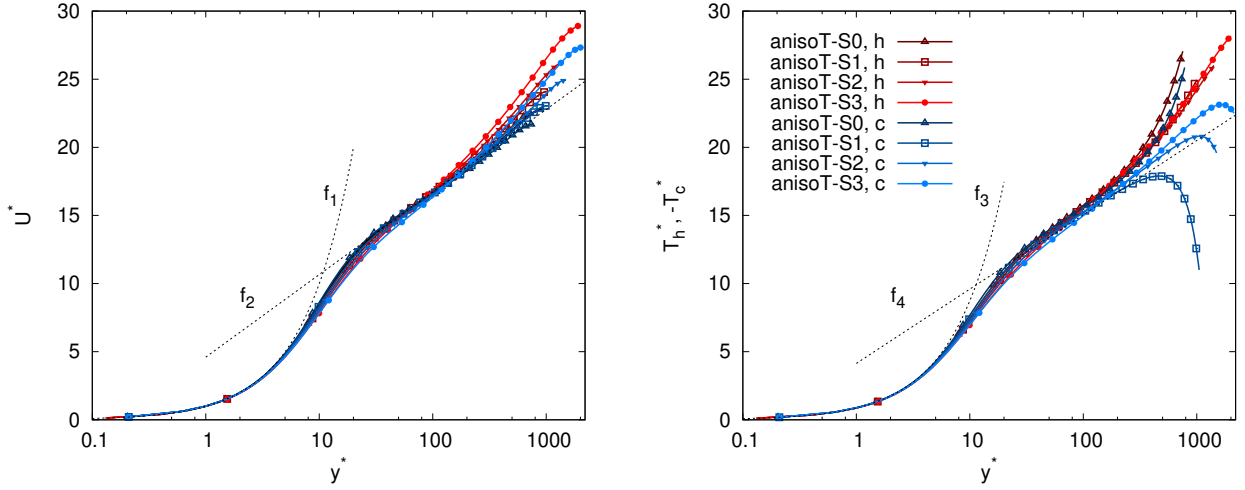


Figure 5: Profiles of streamwise velocity, wall-normal velocity, and temperature normalized with the semi-local scaling.

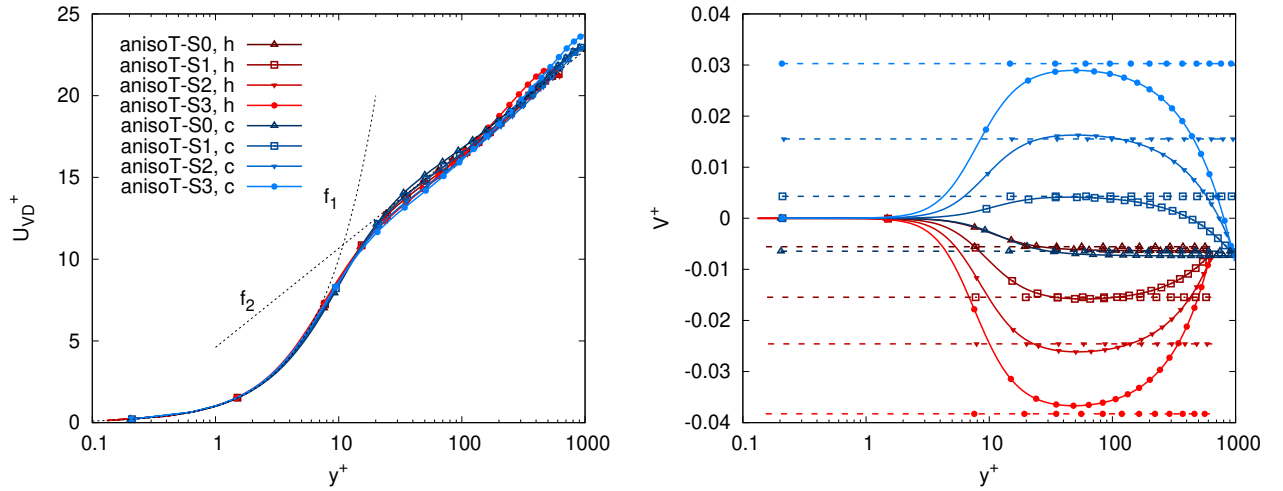


Figure 6: Profiles of streamwise velocity scaled with the Van Driest transformation as well as wall-normal velocity normalized with the wall scaling.

region are modified by the heating. When the heat fluxes are important, the slope is significantly altered. When the wall heat fluxes are high, the wall-normal velocity moves a large amount of fluid toward the center of the channel which is probably responsible for the streamwise velocity increases in the outer layer. Nicoud and Bradshaw (Nicoud and Bradshaw, 2000) express a mathematical analogy between the Van Driest transformation for compressible boundary layers with heat transfer and the Simpson transformation of the velocity profile for incompressible turbulent wall flows with uniform injection (Simpson, 1970). This analogy leads to the following expression of the equivalent injection velocity used in the Van Driest scaling:

$$V_{inj} = Pr_t T_{\tau,w} / T_w U_{\tau,w} \quad (16)$$

The velocity injection is compared to the wall-normal velocity profiles on the right graph. Both velocities are in very good agreement. Toutant and Bataille (Toutant and Bataille, 2013) and Bellec *et al.* (Bellec *et al.*, 2017) also found a good accordance between the equivalent injection velocity and the wall-normal velocity at lower Reynolds numbers and wall heat fluxes.

### 4.3. Second-order statistics

The velocity - velocity, velocity - temperature, and temperature - temperature fluctuations as well as the coefficient correlations are studied in this part.

Figure 7 exhibits the streamwise, spanwise, wall-normal, and cross velocity correlations. Similar behaviors are noticed: fluctuation peaks are higher on the cold side. This is because, the increase of viscosity on the hot side tends to dissipate turbulent kinetic energy. Peak amplitudes are mitigated and located

closer to the wall when the temperature difference increases. The bigger the heat sink, the closer to the wall the maximum energy intensity. This peak shifting is particularly salient for the  $\langle v'v' \rangle^+$  correlation. For instance, the simulation "anisoT-S0" exhibits a peak on the cold side around  $y^+ = 110$  while the equivalent peak of DNS "anisoT-S3" is located at  $y^+ = 60$ . This may be explained by the fact that the increasing of the temperature gradient in the near wall region induces bigger wall-normal velocity which modifies the turbulent structures. For instance, the inclination of low speed streaks is altered (Dong et al., 2022). The wall bursts should occur nearer to the walls when the streamwise velocity is lower. This tends to mitigate the energy transfer and could justify the smaller peak of fluctuations. The  $\langle u'u' \rangle^+$  profiles present peaks in the region  $10 < y^+ < 20$ . It corresponds to the near-wall peak in turbulence production. These peaks are the energetic signature of elongated high- and low-speed regions. Note that, the maximum amplitude is about 1.2 times higher on the cold side than on the hot side for a given simulation due to the lower turbulence level on the last side. For a normalized distance lying between  $y^+ = 50$  and  $y^+ = 300$ , a reduction in the slope is noted. This is due to the large-scale structures that are associated with high turbulence level (Hutchins and Marusic, 2007b). Hence, in the studied conditions, and more significantly for the simulation "anisoT-S3", the energetic peak due to the viscous-scaled near-wall cycle (located at  $y^+ = 15$ ) is contested by much larger outer-scaled events in the logarithmic region (lying between  $y^+ = 50$  and  $y^+ = 300$ ). It is well known that the effects of these last structures become more significant at higher turbulence levels which requires very intensive computational resources (Hutchins and Marusic, 2007a). Here, the presented results show that the second energy peak, which is revealed by the reduction of the slope in the logarithmic region, becomes more important when the gap between the bulk and the wall temperature is high. This can probably be explained by the increase of the bulk Reynolds number when the heat sink grows. Thus, turbulence production spreads out on a significant wall unit range. The cross-correlation exhibits peaks of opposite signs and cancels out on the center line of the channel for all the simulations. The temperature effects only impact the profile amplitude. The four presented graphs point out that the heat transfer direction at the cold wall has no significant influence on the fluctuations aside from the effects due to the reduction of the fluid temperature.

Figure 8 displays the profiles of streamwise and wall-normal velocity correlations normalized with the semi-local scaling. The results indicate that the streamwise velocity fluctuations peaks are closer from each other with this scaling. Significant differences are noticed after  $y^+ = 50$ . The second energy peak clearly increases with the heat sink and thus the Reynolds number. The

significant bump observed for the simulation "anisoT-S3" is directly linked to the increase of the streamwise velocity in the outer layer of the flow (see Figure 5). The profiles of wall-normal velocity fluctuations are significantly different. As observed in Figure 7, the cold side fluctuations are higher than those observed in the hot side. After removing the effects of the mean density and viscosity variations, it appears that the highest fluctuations are obtained for the simulation "anisoT-S3" which is characterized by the highest Reynolds number. The fluctuation profiles of the hot and cold sides do not collapse, which suggests that the turbulence and the temperature gradient interactions are more complex than a simple influence of the fluid property variations. The same observations and conclusions can be made for the spanwise velocity fluctuations (not presented in this paper).

The correlations of velocity - temperature and temperature - temperature are plotted in Figure 9. Focusing on the correlation  $\langle u'\theta' \rangle^o$ , it appears that the simulation "anisoT-S0" has a positive cold side peak contrary to the other simulations. This is because the fluid temperature in the vicinity of the cold wall is higher than the associated wall temperature. The profile cancels on the hot side of the channel at  $y/(2\delta) = 0.52$  due to the influence of the fluid property variations. Indeed, the density is lower in the hot side due to the higher fluid temperature which induces asymmetric streamwise velocity profiles and affects this correlation. The bigger the temperature gradient, the bigger the fluctuation peaks. The same analysis can be performed for the wall-normal turbulent heat flux,  $\langle v'\theta' \rangle^o$ , and the  $\langle \theta'\theta' \rangle^o$  correlations. As expected, the profiles of wall-normal velocity - temperature correlation cancel out in the same location as the wall-normal velocity profiles. The simulation "anisoT-S0" exhibits a central peak of the  $\langle \theta'\theta' \rangle^o$  correlation in addition to the peaks in the vicinity of the walls, also noted by Lyons *et al.* (Lyons et al., 1991). This central peak is due to the combined effects of the temperature gradient and the large turbulence structures in the center of the channel. This is explained by the zero gradient temperature (minimum of the fluid temperature) observed at the normalized location of  $y/(2\delta) = 0.21$ . The minimum temperature fluctuations are seen in the region  $0.08 < y/(2\delta) < 0.21$ . They are due to the combination of low-temperature gradients and weak temperature transport caused by the vicinity of the wall. The two peaks located in the vicinity of the walls are around  $y^+ = 15$ , which is similar to the maximum in the streamwise intensity. For the simulations "anisoT-S2" and "anisoT-S3", the minimum fluid temperature is closer to the center line of the channel, resulting in a minimum of temperature fluctuations around  $y/(2\delta) = 0.35$ .



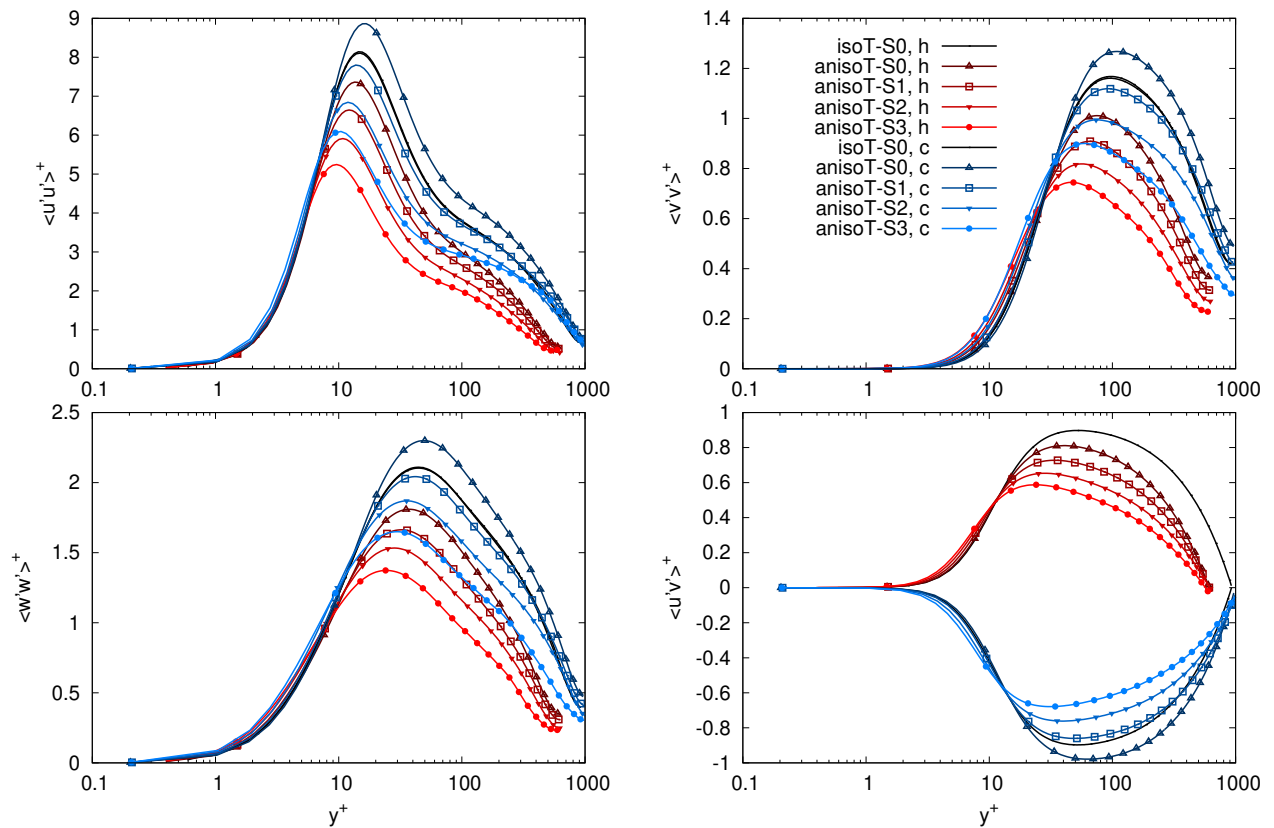


Figure 7: Profiles of velocity fluctuations as functions of the channel height normalized in wall unit.

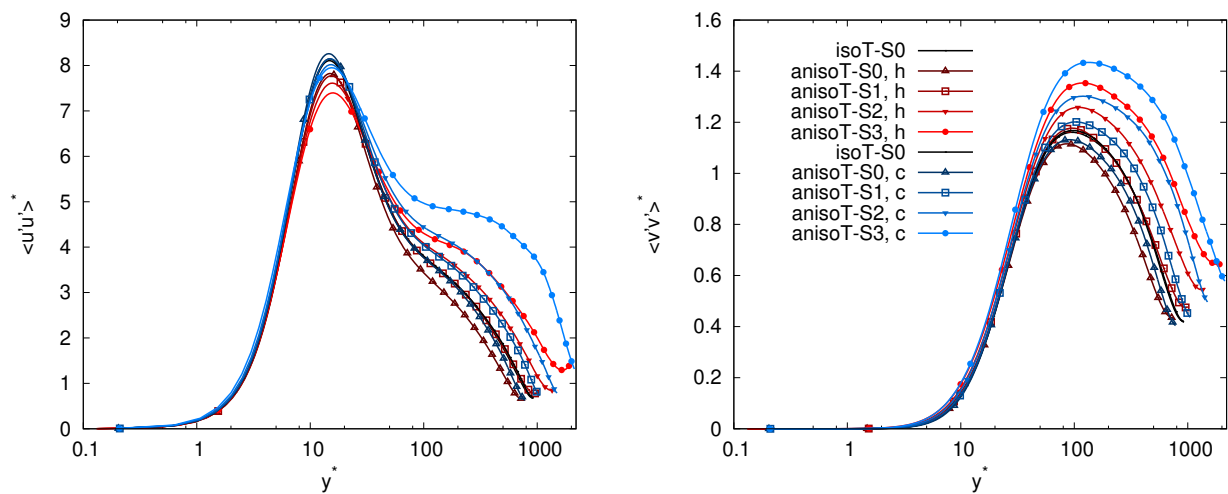


Figure 8: Profiles of velocity fluctuations as functions of the channel height normalized with the semi-local scaling.

Figure 10 presents the profiles of streamwise velocity - temperature correlation and temperature fluctuations normalized with the semi-local scaling. As observed in Figure 8, the semi-local scaling brings closer the fluctuation peaks. The strong asymmetry of the simulation "anisoT-S1" is highlighted on the left graph. Regarding the temperature fluctuations, the results show that the hot and cold profiles of the simulation

performed without a heat sink are almost merged with the semi-local scaling. This is not observed for the other simulations which traduces the strong influence of the heat fluxes on the profiles. The semi-local scaling allows the hot side temperature fluctuations to be higher than the cold side ones, contrary to what is observed on the velocity fluctuations. This is because the higher velocity

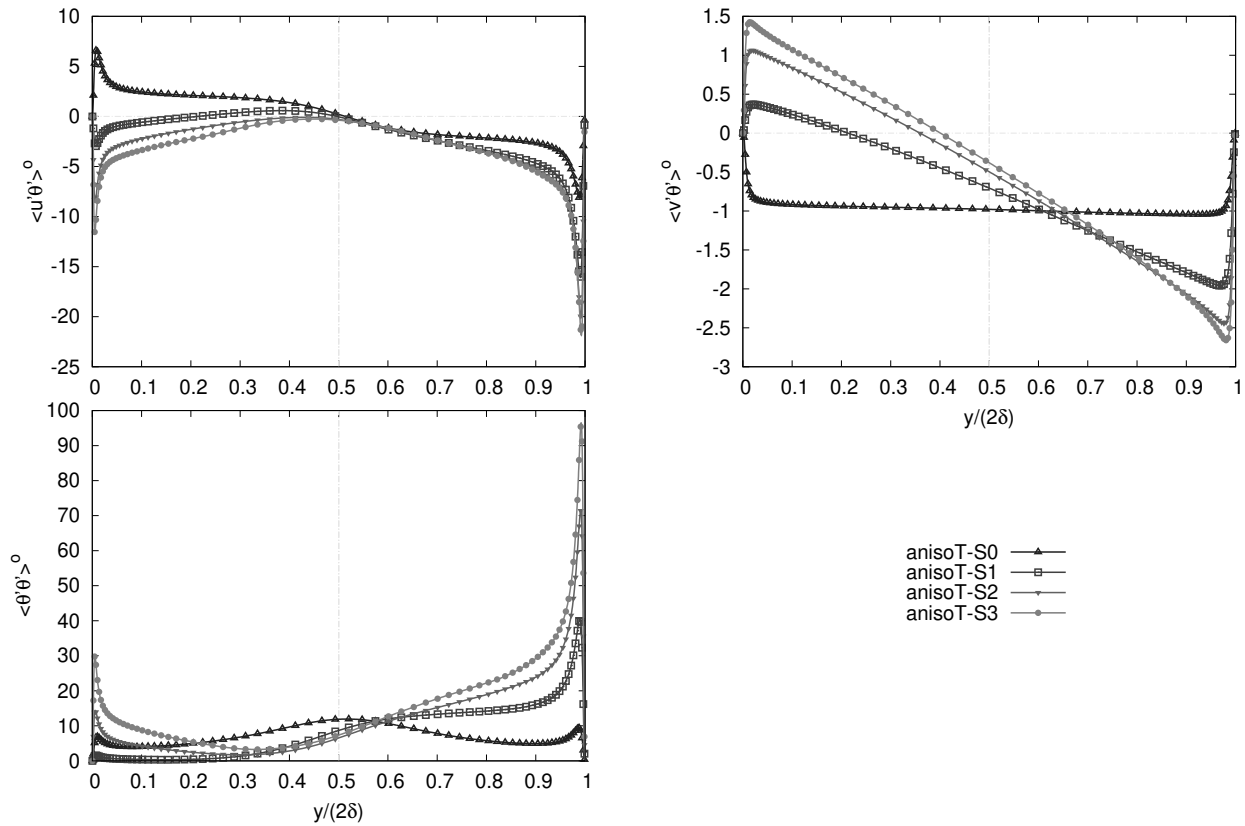


Figure 9: Profiles of velocity - temperature correlations and temperature fluctuations as functions of the normalized channel height.

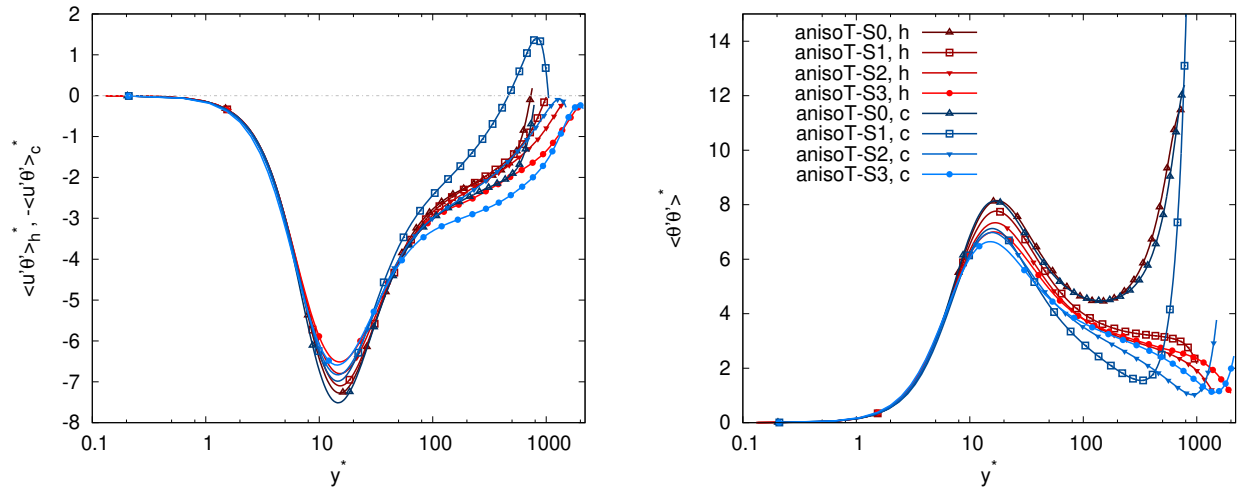


Figure 10: Profiles of streamwise velocity - temperature correlation and temperature fluctuations normalized with the semi-local scaling.

fluctuations induce more efficient mixing, resulting in more homogeneous temperature fields.

The fluctuations of wall heat fluxes and wall friction are exposed in Table 4. The results point out that the fluctuations increase with the mean value. The ratio between the wall heat flux fluctuations and the mean

wall heat flux is about 0.44 at both walls for all the simulations. It slightly increases for the DNS performed with the biggest heat sink. Regarding the wall friction, similar tendencies are observed. Notice that, the normalized fluctuations of wall friction are somewhat weaker than the ones of wall heat fluxes. Kim and

Moin (Kim and Moin, 1989) have found a ratio of 0.38 studying the transport of passive scalar in turbulent channel flow at a friction Reynolds number of 180. Note that the non-monotonic trend of the fluctuations of wall friction with respect to the symmetrical might be explained by the insufficiency of ensemble averaging.

Figure 11 plots the profiles of velocity - temperature coefficient correlations. The two presented graphs highlight the fact that the profile on the cold side is significantly modified by the temperature distribution. On the left graph, when the cold wall heats the fluid, the term  $\langle u'\theta' \rangle$  is negative. As the fluid temperature grows, the observed bell shape profiles get bigger and become closer to the profile performed without a heat sink. Thus, the top of the bell shape is shifted toward the cold wall as the gap between the fluid temperature and the cold wall temperature is reduced. A singularity in the coefficient sign at the cold wall should appear when the wall heat flux becomes null accordingly to what has been observed by Kuznetsov and Nield on the Nusselt number (Kuznetsov and Nield, 2010). The amplitudes of the correlation coefficient are close to 1 in the vicinity of the walls, meaning that the scalar field is highly correlated with the streamwise velocity in the viscous wall region. This is in good agreement with Lyons *et al.* (Lyons *et al.*, 1991) observations. Regarding the right graph, it appears that the coefficient correlation involving the wall-normal velocity is lower than the one involving the streamwise velocity. This was also observed by Kim and Moin (Kim and Moin, 1989) and Orlandi *et al.* (Orlandi *et al.*, 2016) in passive scalar transport conditions. The coefficient cancels out closer to the cold wall when the heat sink is weaker. The asymmetry of the coupling between the dynamic and the temperature is then increased for small temperature differences between the cold wall and the fluid. This is in agreement with the observations carried out on heat flux fluctuations, see Table 4. On the hot side, the profiles are similar between all the simulations, meaning that the correlation between velocity and temperature is poorly influenced by the hot wall heat flux.

The turbulent Prandtl number is defined by:

$$Pr_t = \frac{\nu_t}{\alpha_t} = \frac{\langle u'v' \rangle \partial \langle T \rangle / \partial y}{\langle v'\theta' \rangle \partial \langle U \rangle / \partial y}, \quad (17)$$

with  $\alpha_t$  the turbulent diffusivity for heat. Figure 12 shows the turbulent Prandtl number profiles. The profiles are rather scattered because of the strong variations due to the streamwise velocity and temperature derivatives that cancel out in the center area of the channel. The results indicate that it can be relatively well approximated by 0.9. This is conforming with Kays (Kays, 1994). The turbulent Prandtl number profiles display peaks between  $y^+ = 30$  and  $y^+ = 50$ , also observed in (Toutant and Bataille, 2013). Singularities are observed near the center of the channel due to the null streamwise velocity gradient.

The profiles of the turbulent kinetic energy production ( $Prod = \langle u'v' \rangle \partial U / \partial y$ ) normalized with the semi-local scaling are given by

$$Prod^* = Prod / (U_{\tau,w}^{4,*} / \nu(y)). \quad (18)$$

They are plotted on Figure 13. For a given side, the production profiles are almost merged. They exhibit peaks in the near wall region, as classically observed in the isothermal case. The cold peak is higher than the hot one. It is due to the different wall temperatures that induce variations in the fluid properties and affect the turbulence production. This term explain the higher turbulence levels observed on the cold side than on the hot side.

#### 4.4. Instantaneous fields

In this subsection, the coupling between the wall heat flux and the wall friction is firstly visualized with heat maps then it is quantified thanks to probability density functions (PDF) and spectral analyzes to provide a deep understanding of these interactions.

In Figure 14, the quantities are normalized with the associated standard deviation. On the left graphs, respectively right graphs, the results are those of the hot wall, respectively cold wall. The legend is adapted for each instantaneous field to facilitate the reading:

$$\frac{X_{w,maxplotted}}{X_{w,rms}} = \frac{X_{w,mean}}{X_{w,rms}} + 3.9 \quad (19)$$

where  $X$  is either the wall heat flux or the wall friction.

The patterns observed at the cold wall are similar to those of the hot wall but they are smaller. This is due to the lower turbulence level on the hot side that is explained by the higher temperature of the hot wall, and thus, the higher kinematic viscosity. Similar results are observed in the works of Kawamura *et al.* (Kawamura *et al.*, 1999) and Abe *et al.* (Abe *et al.*, 2004), which deal with the study of passive scalar in turbulent channel flows. High wall heat fluxes are associated with small circular structures whereas low wall heat fluxes are characterized by elongated structures in the streamwise direction. The regions of high wall heat flux coincide with those of high-speed fluid whereas the regions covered by the low-speed streaks are associated with low heat transfer or low wall friction. This is conforming to the results of Kim and Moin (Kim and Moin, 1989). The instantaneous fields of wall friction are close to those of wall heat flux but they exhibit some discrepancies. Indeed, the results indicate that small circular regions of very low wall friction appear in elongated structures which are not observed in the wall heat flux fields. The bottom graphics show areas of higher normalized wall heat flux that are either circular or elongated in the spanwise direction.

Simulation	$\phi_{rms}^h$ [kW/m <sup>2</sup> ]	$\phi_{rms}^c$ [kW/m <sup>2</sup> ]	$\phi_{rms}^h/\phi^h$	$\phi_{rms}^c/\phi^c$	$\tau_{rms}^h$ [Pa]	$\tau_{rms}^c$ [Pa]	$\tau_{rms}^h/\tau^h$	$\tau_{rms}^c/\tau^c$
anisoT-S0	42.0	42.0	0.43	0.43	17.6	19.7	0.40	0.41
anisoT-S1	112.3	27.1	0.43	0.43	17.6	19.5	0.41	0.41
anisoT-S2	194.8	104.4	0.44	0.43	17.5	20.2	0.42	0.43
anisoT-S3	262.8	187.5	0.45	0.46	16.7	19.5	0.42	0.44

Table 4: Wall heat flux and wall friction fluctuations.

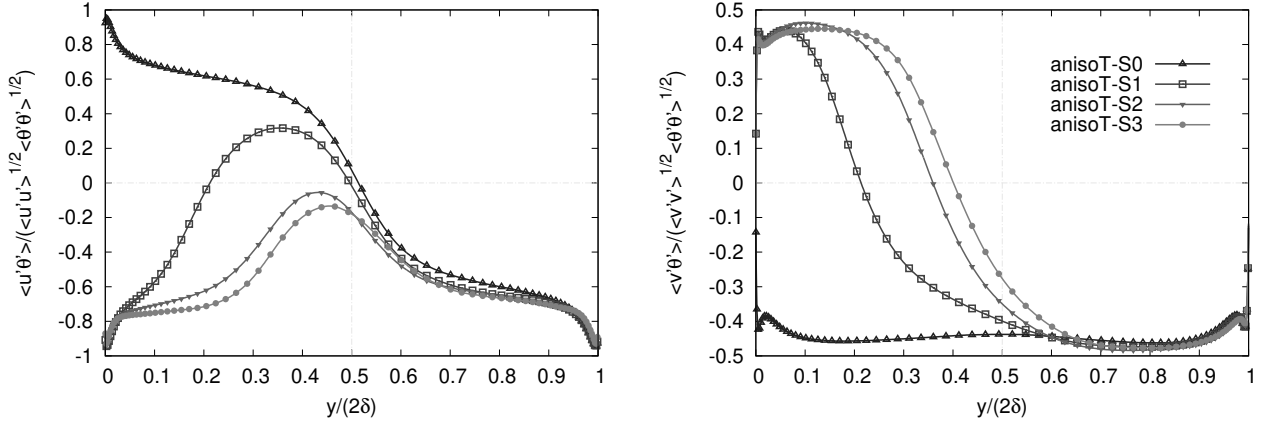


Figure 11: Profiles of velocity - temperature coefficient correlations as functions of the normalized channel height.

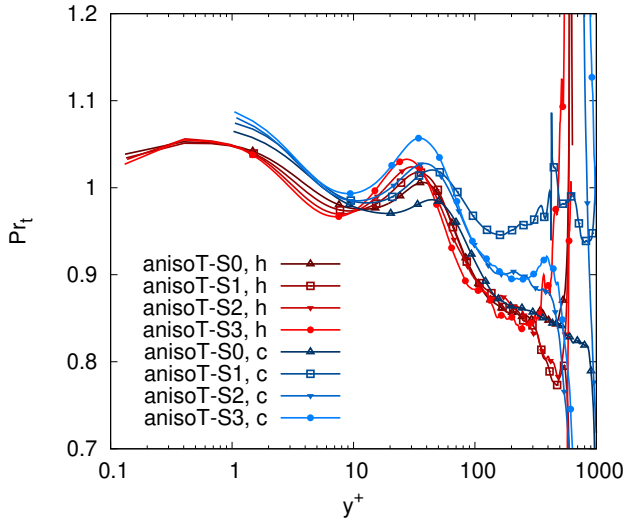


Figure 12: Profiles turbulent Prandtl number.

The probability density of wall heat flux and wall friction are exposed in Figure 15. They are defined by:

$$\int_0^{X_{max}} PDF(X_w) dX_w = 1, \quad (20)$$

where  $X$  is either the wall heat flux or the wall friction. All the simulations exhibit similar profiles of PDF. However, the minimum wall heat flux is  $0.23\phi_{mean}$  while the minimum wall friction is 0. The results

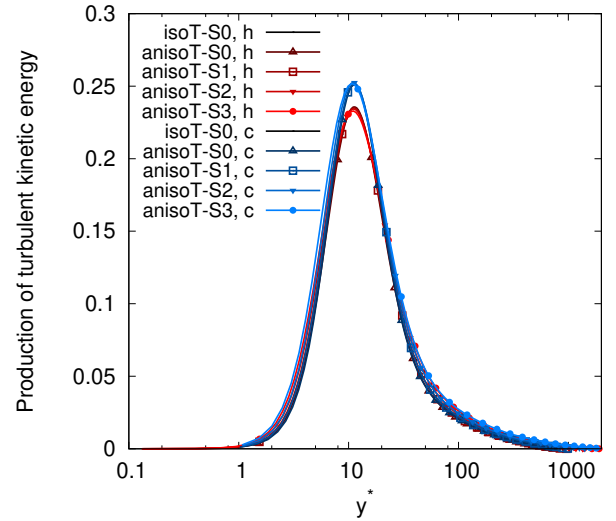


Figure 13: Profiles of the turbulent kinetic energy production as functions of the normalized channel height. The results are normalized with the semi-local scaling.

highlight that all the peaks of PDF are located at  $\phi/\phi_{mean} - 1 = -0.34$  and around  $\tau/\tau_{mean} - 1 = -0.28$ . They correspond to the most frequent wall heat fluxes or wall frictions. It seems that the hot peaks of wall friction are very slightly shifted toward 0 when compared to the cold peaks. The PDF peak of wall heat

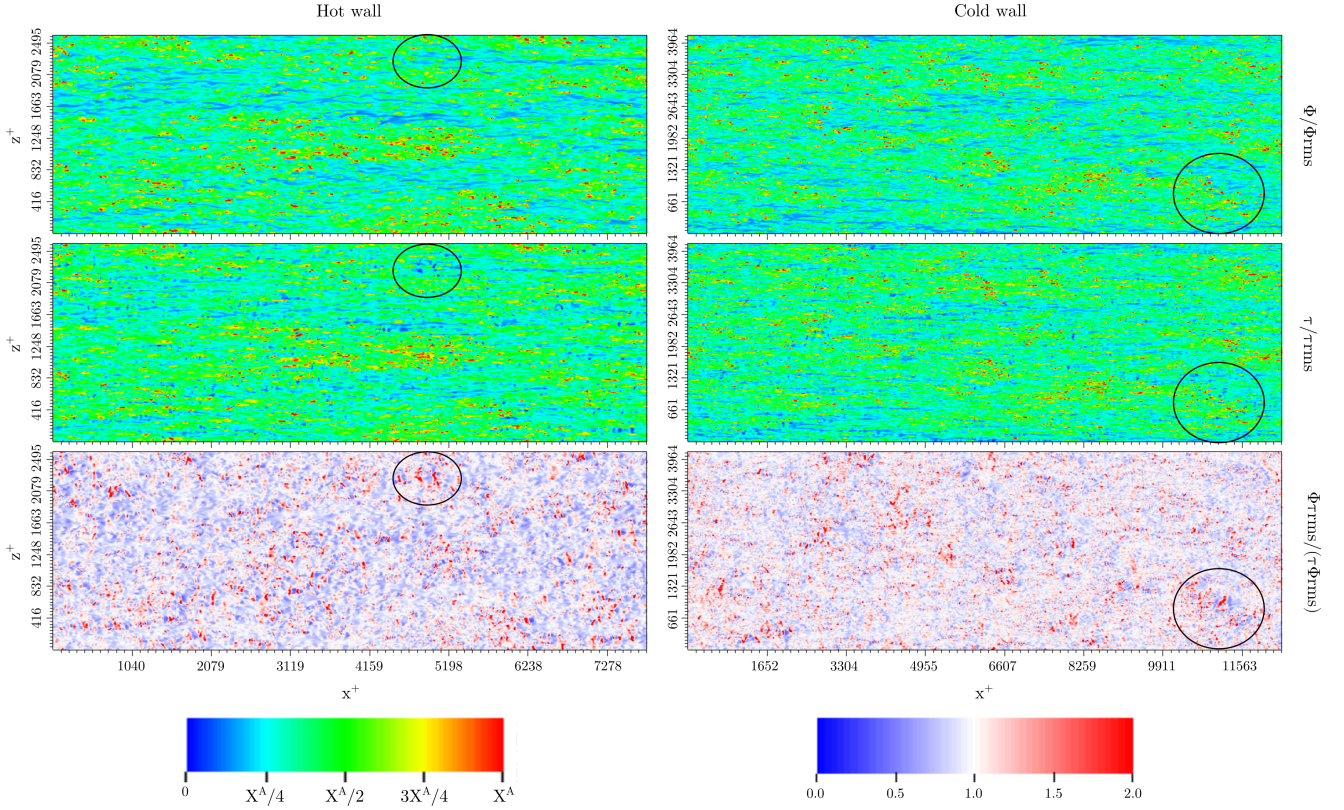


Figure 14: Instantaneous fields of normalized wall heat flux and wall friction as well as the ratio between the two quantities. The presented results are those of the DNS "anisoT-S3". The left legend is associated with the graphics of the two first lines and the right legend is associated with the graphics of the last line. The symbol  $X^A$  either denotes the wall heat flux or the wall friction depending on the observed line of graph.

flux is mitigated when the heat transfer is increased. For a given wall heat flux, the PDF peak is lower when the turbulence level is higher (see curves corresponding to hot and cold sides of the simulation "anisoT-S0"). This is because, the maximum wall heat flux grows with the friction Reynolds number. No clear behavior appears when regarding the amplitude of the wall friction PDF.

The obtained density probability function can be well interpolated with skewed Gaussian distribution, see dashed lines in the Figure 15, which expression is given by:

$$f(x) = \frac{A}{\beta\sqrt{2\pi}} e^{\left[-\frac{(x-\mu)^2}{2\beta^2}\right]} \left[1 + \operatorname{erf}\left(\frac{\gamma(x-\mu)}{\beta\sqrt{2}}\right)\right] \quad (21)$$

with  $\operatorname{erf}$  the error function,  $A$  the amplitude parameter,  $\mu$  the location parameter,  $\beta$  the scale parameter, and  $\gamma$  the shape parameter. The results of the interpolation are presented in Figure 15 with dashed lines. They have been obtained with the parameters listed in Table 5.

Figure 16 is obtained by extracting data along the center line in the streamwise direction of Figure 14 for the top graph and along the center line in the spanwise direction of Figure 14 for the bottom graph. It permits performing a quantitative analysis of the spatial distribution of the wall heat flux and the wall

friction. As explained above, the wall heat flux and wall friction fields are similar. Most of the peaks are gathered in groups and distributed quite evenly in each group with a distance of between  $x^+ = 200$  and  $x^+ = 500$ . The regions of low heat flux regions are sometimes associated with sharp peaks of very low wall friction. Regarding the bottom graph, it appears that the peaks are closer to each other. The distance between peaks is lying between  $z^+ = 100$  and  $z^+ = 200$ . This is because the main structures are elongated in the streamwise direction. The peaks are well distributed and it seems that there is no gathering of structures in this direction.

In the next, 1D spectra of turbulent kinetic energy, power, and friction are discussed. Discrete Fourier transforms of these quantities are performed along lines oriented in the streamwise or spanwise direction. There are as many lines as grid points in the considered direction. For each simulation and each variable, the discrete Fourier transform is conducted over three independent instantaneous fields. Furthermore, a Bezier interpolation is performed to improve the reading of spectra. The spectral terms depend on  $k_x$  or  $k_z$ , the wave number in the streamwise or spanwise direction. In the following graphs, the wave number is normalized in wall unit,  $k_x^+ = k_x U_{\tau,w} / \nu_w$  and  $k_z^+ = k_z U_{\tau,w} / \nu_w$ .



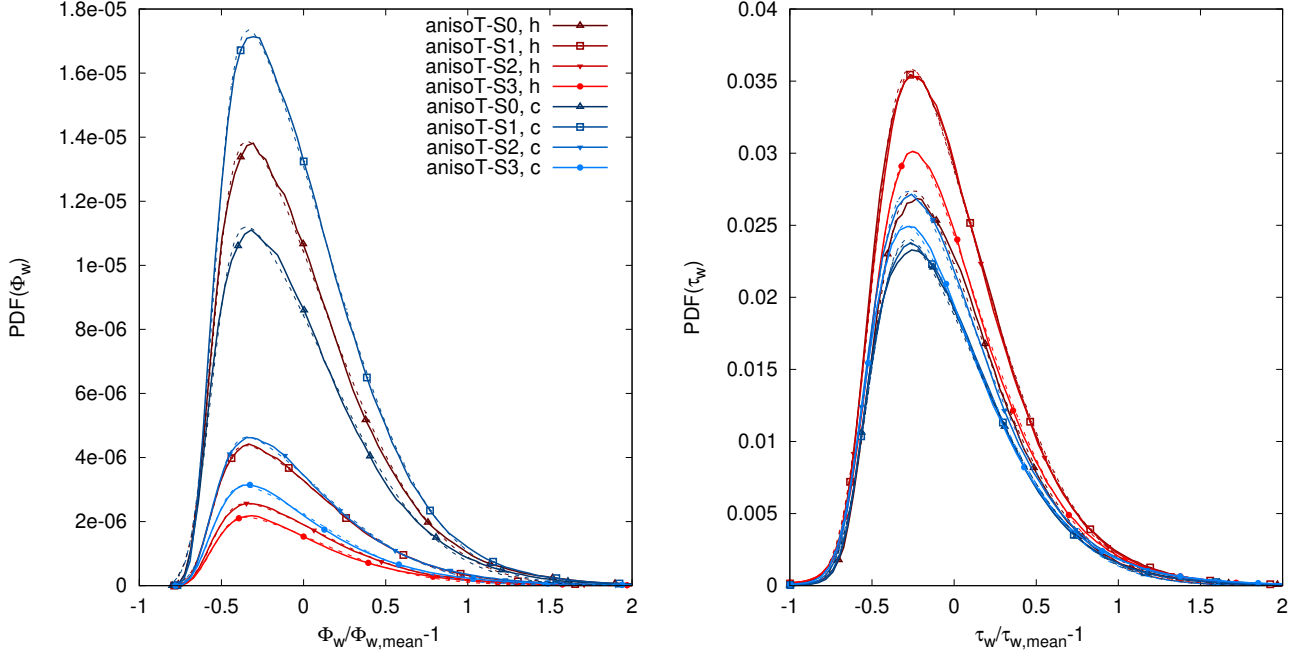


Figure 15: Probability density functions of wall heat fluxes and wall frictions. Dashed lines stand for the curve interpolations with skewed Gaussian distributions. The parameters used to fit the PDF are given in appendix.

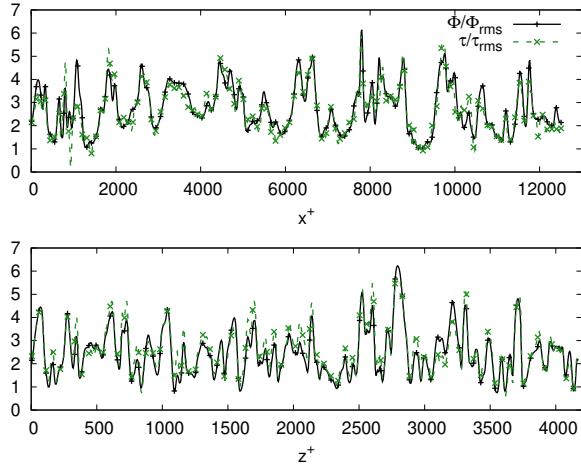


Figure 16: Normalized wall heat flux and wall friction at the cold wall of the simulation "anisoT-S3" as functions of the streamwise location (top graph) or the spanwise location (bottom graph).

The turbulent kinetic energy spectra are given by:

$$\int_0^{+\infty} E(k_{x_i}) dk_{x_i} = \frac{1}{2} (u_{rms}^2 + v_{rms}^2 + w_{rms}^2), \quad (22)$$

where  $k_{x_i}$  is either  $k_x$  or  $k_z$ . In Figure 17, the turbulent kinetic energy spectra in the streamwise direction are investigated at a normalized distance of  $y^+ = 40$ . The spectra diminish on the whole studied range of

wavenumber. The curves are divided into two groups, each one corresponding to a side. The isothermal simulation presents similar results to the cold wall turbulent kinetic energy spectra. It appears that the turbulence level is clearly impacting those results. The transition between the inertial zone and the energy dissipation zone is observed for lower wavenumber at high friction Reynolds numbers. It seems that, for a given wall and wavenumber, the higher the wall heat fluxes are, the wider the inertial range and the bigger the energy level in the energy dissipation range. The obtained slope in the dissipation zone is too sharp. Vreman *et al.* (Vreman et al., 2014) compared DNS energy spectra obtained with finite difference algorithms and spectral algorithms. They show that the energy spectrum in the streamwise direction falls off too sharply when the finite difference algorithm is used. This may be due to the finite difference operator in the convective terms that behaves like an implicit filter over the nonlinear transfer to the highest wavenumbers. Notice that this error only affects the streamwise energy spectra and is limited to the smallest scales. The integrals of the energy spectra remain valid.

Figure 18 presents the turbulent kinetic energy spectra in the spanwise direction. On these spectra, a maximum of energy is observed at  $k_z^+ = 0.0020$  for the cold side and  $k_z^+ = 0.0035$  for the hot side. Hence, the highest values are obtained for wider turbulent structures when the turbulence level is higher. The energy levels are lower than those observed in Figure 17.

The inertial range is thinner for 1D spectra in the spanwise direction than for 1D spectra in the spanwise direction. The dissipation range is characterized by a small slope when compared to the results of 1D spectra in the spanwise direction. The slopes in the dissipation zone approximately follow a  $-6$  power law which is consistent with the results commonly observed in the literature, see Refs. (Kim et al., 1987; Moser et al., 1999; Vreman et al., 2014).

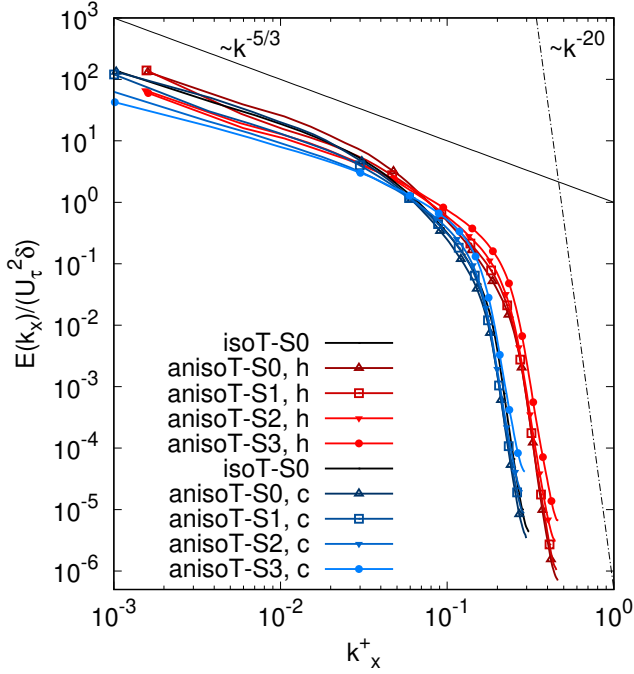


Figure 17: Turbulent kinetic energy spectra in the streamwise direction at  $y^+ \approx 40$ .

The power and the friction spectra in the streamwise direction are respectively defined by:

$$\int_0^{+\infty} P(k_{x_i}) dk_{x_i} = \frac{1}{2} \phi_{rms}^2 \quad (23)$$

and

$$\int_0^{+\infty} F(k_{x_i}) dk_{x_i} = \frac{1}{2} \tau_{rms}^2, \quad (24)$$

where  $k_{x_i}$  is either  $k_x$  or  $k_z$ .

Spectral analysis of the wall heat fluxes and the wall frictions permits identifying the size of the turbulent structures that have to be enhanced to maximize the heat transfer while minimizing the wall friction. Thus it permits adjusting the pattern of textured surface (Daguenet-Frick et al., 2012) or the frequency of oscillating walls (Rittidech and Wannapakne, 2007) to optimize solar receivers. To the author's knowledge, there are very few spectral analyzes of these quantities in the literature.

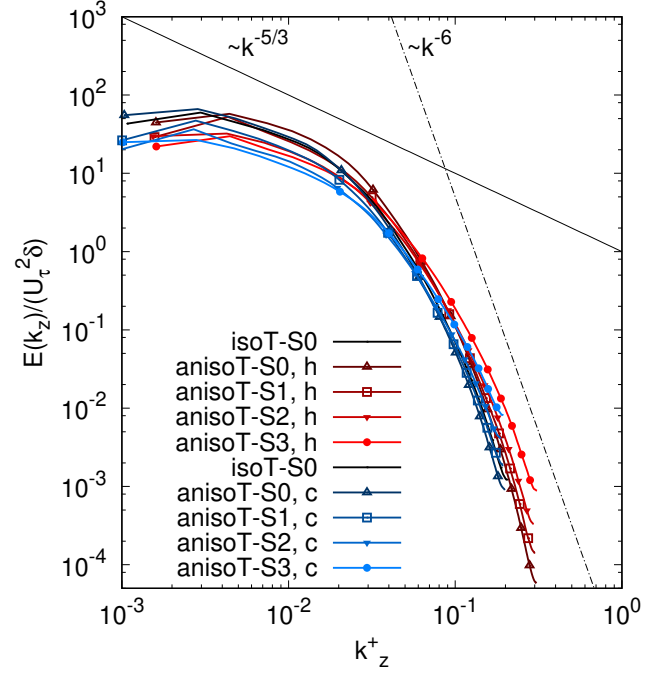


Figure 18: Turbulent kinetic energy spectra in the spanwise direction at  $y^+ \approx 40$ .

Figure 19 plots the power and friction spectra as well as the ratio between the two quantities at hot and cold walls for all the performed anisothermal simulations, excepted "anisoT-S2" to facilitate the reading. The power and friction spectra exhibit similar tendencies that the classically studied turbulent kinetic energy spectra. The slope of the energy transfer is proportional to  $k_x^{-5/3}$  in the inertial zone then energy is dissipated with a slope proportional to  $k_x^{-7}$ . The same turbulence level and wall heat flux effects are observed in Figure 17. When observing the ratio between the power and friction spectra it appears that for low wavenumber the wall heat flux spectra are slightly lower than the wall friction spectra at the cold wall. A peak is observed in the range  $0.03 < k_x^+ < 0.05$ , corresponding to  $126 < x^+ < 210$ . It seems that the heat transfer is significantly favored in this range for all the studied configurations. The higher the wall heat flux, the bigger the wavenumber associated with the peak. When the wavenumber is higher than  $k_x^+ = 0.08$  for the cold wall, and lower than  $k_x^+ = 0.1$  for the hot wall, the normalized power spectra are lower than the normalized friction spectra. For the last region, which corresponds to the highest wavenumber values for each simulation, the results have to be interpreted with caution because of the effects of the numerical setup. Sharp oscillations are noted. For the simulation "anisoT-S0", the normalized wall heat flux spectrum

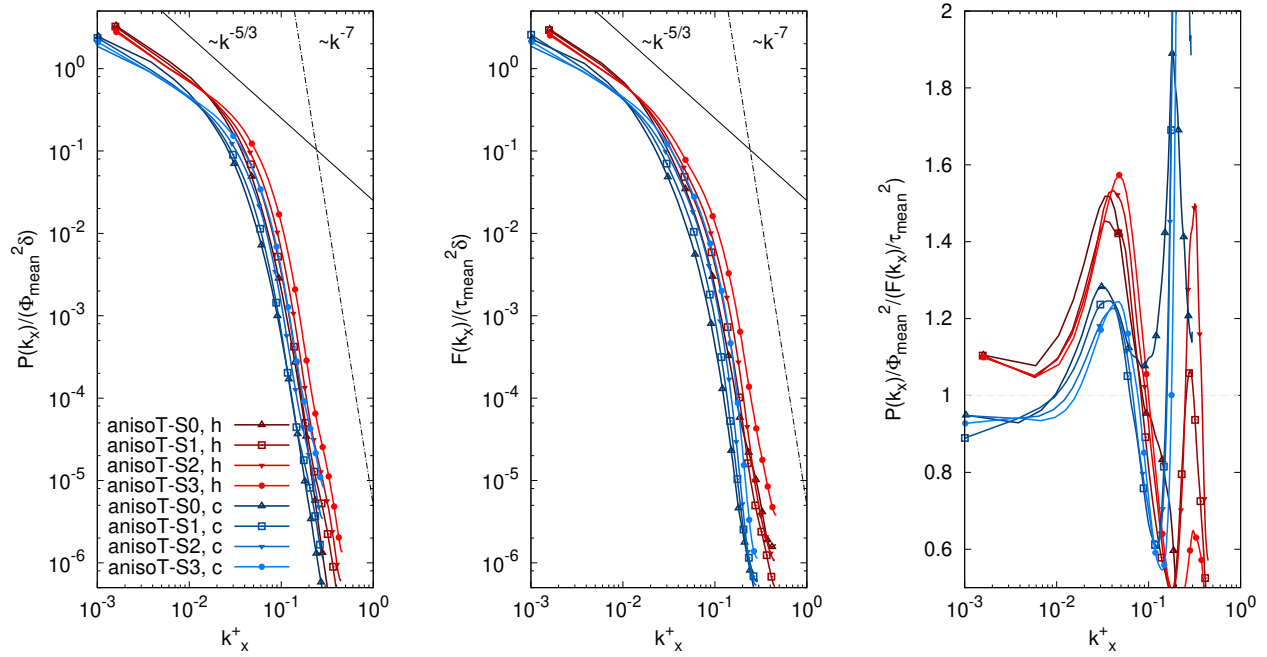


Figure 19: Power and friction spectra in the streamwise direction at the walls.

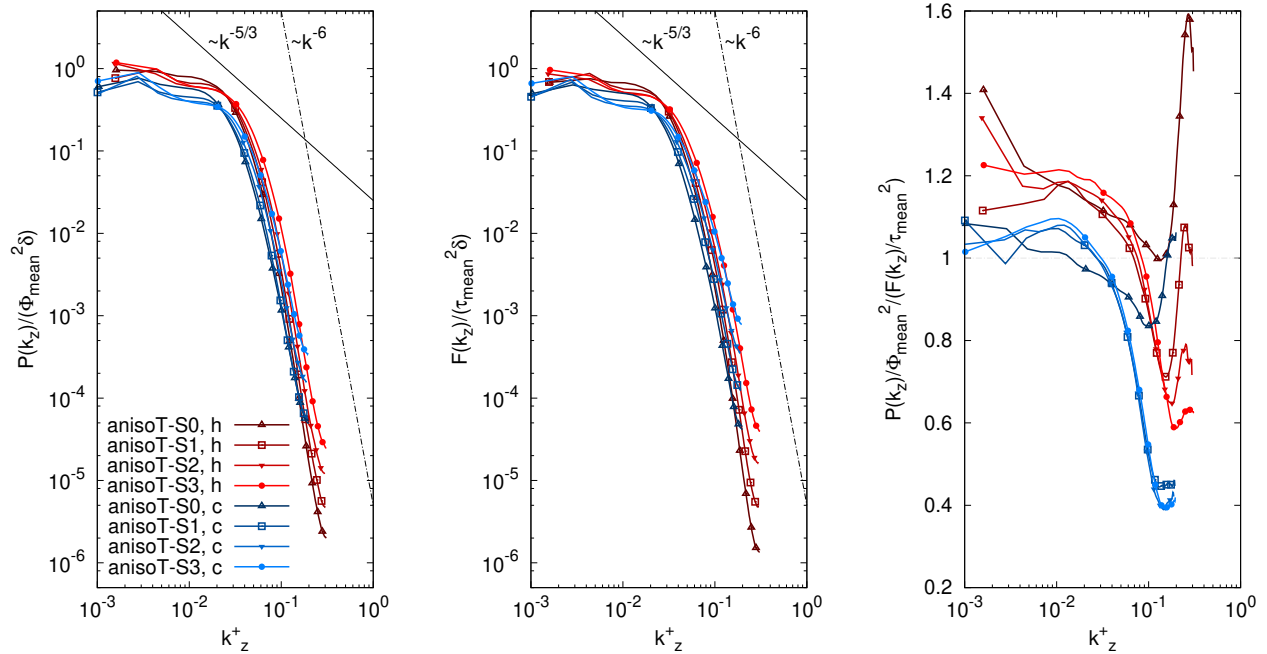


Figure 20: Power and friction spectra in the spanwise direction at the walls.

remains higher than the normalized wall friction spectrum. This might be because in this particular case, the cold wall is cooling the fluid.

In Figure 20, the power and friction spectra in the spanwise direction at the walls are studied. The same discrepancies that are listed in the comparison

of Figure 17 and Figure 18 can be noticed between Figure 19 and Figure 20. The results are conforming to those presented in (Abe et al., 2004). Regarding the right graph, it appears that there is no evident structure size that should be forced to enhance heat transfer while keeping low-pressure losses. Nevertheless, it seems that,



globally, largest structures in the spanwise direction should be promoted. This is in agreement with the elongated red stains observed on the bottom graph of Figure 14. Once again, a sharp drop in the ratio is noted. The decrease occurs for smaller normalized wavenumbers at the cold wall ( $k_z^+ \approx 0.03$ ) than at the hot wall ( $k_z^+ \approx 0.08$ ).

## 5. Conclusions

In this study, four DNS of anisothermal channel flow have been carried out in the operating conditions of gas-pressurized solar receivers. The fluid properties are dependent on the temperature. The wall temperature and the mean wall friction are the same for all the simulations but the temperature profile is modified to investigate different locations in the absorber. The coupling between the dynamic and the temperature has been analyzed. Careful attention is paid to the comparison between the wall heat fluxes and the wall frictions.

The results indicate that the fluid temperature significantly impacts the streamwise and wall-normal velocities. The wall-normal velocity can be well approximated with the equivalent injection velocity. The Van Driest transformation does not allow the hot and cold mean velocity profiles to exactly collapse but provides a good profile merging. The velocity fluctuations are also affected by the temperature. Neither the wall nor the semi-local scaling allows the hot and cold velocity fluctuations to match. When the fluid temperature is reduced the main peak of fluctuations is mitigated and the second energy peak becomes more important meaning that the turbulence production spreads out. The fluctuations of wall heat flux and the wall friction normalized by their mean value weakly depend of the fluid temperature distribution. The normalized fluctuations of wall heat flux are slightly higher than those of wall friction. The near-wall peaks of temperature fluctuations are amplified when the wall heat flux increases. The asymmetric heating of the fluid by both walls completely modifies the profile of temperature fluctuation. The streamwise velocity fluctuations and the temperature fluctuations are highly correlated in the vicinity of the walls. The study of the instantaneous fields points out that the wall heat flux patterns are close to those of wall friction. However, the wall friction fields exhibit small structures associated with very low frictions that do not appear when regarding the wall heat flux results. The higher temperature of the hot wall mitigates the turbulence level which conducts to bigger turbulent structures in the vicinity of the hot wall when compared with the cold side. The probability density functions have been investigated. The results show that the most common wall heat flux and wall friction are inferior to the mean value. Skewed Gaussian models fit very well the distribution

of these quantities. One dimensional spectral analyzes in the streamwise and spanwise directions of wall heat flux and wall friction permit quantifying the effects of turbulence level and wall heat fluxes. The discrepancies and similarities between wall heat flux and wall friction are discussed. This could help identify the structures that have to be amplified to optimize solar receivers. The results highlight that the structures that are in the range  $126 < x^+ < 210$  and that are elongated in the spanwise direction should be generated to enhance heat transfer in the studied conditions. It signifies that heat transfer enhancement devices have to be adapted to each wall.

## Appendix - Parameters used to fit the PDF

Figure 15 presents the PDF of wall heat fluxes and wall frictions. Each curve is approximated thanks to a skewed Gaussian distribution. The used parameters are given in Table 5.

## Acknowledgments

This work was granted access to the HPC resources of CINES under the allocation 2022-A0112A05099 made by GENCI. The authors gratefully acknowledge the CEA for the development of the TRUST platform.

## CRedit authorship contribution statement

**Martin David:** Conceptualization, Methodology, Investigation, Data acquisition, Writing. **Adrien Toutant:** Work guiding, Reviewing. **Françoise Bataille:** Work guiding, Reviewing.

## References

- IEA. Concentrated Solar Power (CSP) – Analysis. URL <https://www.iea.org/reports/concentrated-solar-power-csp>.
- IRENA. Renewable Power Generation Costs in 2020. URL <https://www.irena.org/publications/2021/Jun/Renewable-Power-Costs-in-2020>.
- H. Abe and R. A. Antonia. Mean temperature calculations in a turbulent channel flow for air and mercury. *International Journal of Heat and Mass Transfer*, 132:1152–1165, Apr. 2019.
- H. Abe, H. Kawamura, and Y. Matsuo. Surface heat-flux fluctuations in a turbulent channel flow up to  $Re\tau=1020$  with  $Pr=0.025$  and  $0.71$ . *International Journal of Heat and Fluid Flow*, 25(3):404–419, June 2004.
- F. Alcántara-Ávila and S. Hoyas. Direct numerical simulation of thermal channel flow for medium–high Prandtl numbers up to  $Re\tau=2000$ . *International Journal of Heat and Mass Transfer*, 176:121412, Sept. 2021.
- F. Alcántara-Ávila, S. Hoyas, and M. J. Pérez-Quiles. DNS of thermal channel flow up to  $Re\tau=2000$  for medium to low Prandtl numbers. *International Journal of Heat and Mass Transfer*, 127:349–361, Dec. 2018.
- F. Aulery, D. Dupuy, A. Toutant, F. Bataille, and Y. Zhou. Spectral analysis of turbulence in anisothermal channel flows. *Computers & Fluids*, 151:115–131, June 2017.

Simulation	Parameter	$PDF(\phi^h)$	$PDF(\phi^c)$	$PDF(\tau^h)$	$PDF(\tau^c)$
anisoT-S0	$A$	$3.77 \times 10^{-02}$	$3.99 \times 10^{-02}$	$2.96 \times 10^{-02}$	$4.34 \times 10^{-02}$
	$\mu$	$-5.55 \times 10^{-01}$	$-5.62 \times 10^{-01}$	$-4.99 \times 10^{-01}$	$-5.25 \times 10^{-01}$
	$\sigma$	$6.54 \times 10^{-01}$	$6.63 \times 10^{-01}$	$6.11 \times 10^{-01}$	$6.30 \times 10^{-01}$
	$\gamma$	$6.39 \times 10^{+00}$	$6.37 \times 10^{+00}$	$4.23 \times 10^{+00}$	$4.71 \times 10^{+00}$
anisoT-S1	$A$	$3.46 \times 10^{-02}$	$3.83 \times 10^{-02}$	$3.63 \times 10^{-02}$	$4.29 \times 10^{-02}$
	$\mu$	$-5.55 \times 10^{-01}$	$-5.44 \times 10^{-01}$	$-5.10 \times 10^{-01}$	$-5.21 \times 10^{-01}$
	$\sigma$	$6.55 \times 10^{-01}$	$6.47 \times 10^{-01}$	$6.18 \times 10^{-01}$	$6.24 \times 10^{-01}$
	$\gamma$	$6.70 \times 10^{+00}$	$6.39 \times 10^{+00}$	$4.36 \times 10^{+00}$	$4.55 \times 10^{+00}$
anisoT-S2	$A$	$4.06 \times 10^{-02}$	$3.31 \times 10^{-02}$	$3.84 \times 10^{-02}$	$4.30 \times 10^{-02}$
	$\mu$	$-5.54 \times 10^{-01}$	$-5.48 \times 10^{-01}$	$-5.04 \times 10^{-01}$	$-5.26 \times 10^{-01}$
	$\sigma$	$6.43 \times 10^{-01}$	$6.39 \times 10^{-01}$	$6.09 \times 10^{-01}$	$6.21 \times 10^{-01}$
	$\gamma$	$6.52 \times 10^{+00}$	$6.49 \times 10^{+00}$	$4.10 \times 10^{+00}$	$4.51 \times 10^{+00}$
anisoT-S3	$A$	$3.85 \times 10^{-02}$	$4.43 \times 10^{-02}$	$3.35 \times 10^{-02}$	$4.67 \times 10^{-02}$
	$\mu$	$-5.55 \times 10^{-01}$	$-5.60 \times 10^{-01}$	$-5.06 \times 10^{-01}$	$-5.39 \times 10^{-01}$
	$\sigma$	$6.29 \times 10^{-01}$	$6.29 \times 10^{-01}$	$6.09 \times 10^{-01}$	$6.25 \times 10^{-01}$
	$\gamma$	$6.43 \times 10^{+00}$	$6.58 \times 10^{+00}$	$4.12 \times 10^{+00}$	$4.58 \times 10^{+00}$

Table 5: Parameters used to fit the wall heat flux and wall friction PDF with skewed Gaussian distributions.

- D. Dupuy, A. Toutant, and F. Bataille. A posteriori tests of subgrid-scale models in strongly anisothermal turbulent flows. *Physics of Fluids*, 31(6): 065113, June 2019.
- A. W. Vreman and J. G. M. Kuerten. Comparison of direct numerical simulation databases of turbulent channel flow at  $Re\tau = 180$ . *Physics of Fluids*, 26(1): 015102, Jan 2014.
- J. M. Avellaneda, F. Bataille, and A. Toutant. DNS of turbulent low Mach channel flow under asymmetric high temperature gradient: Effect of thermal boundary condition on turbulence statistics. *International Journal of Heat and Fluid Flow*, 77: 40–47, June 2019.
- M. Bellec, A. Toutant, and G. Olalde. Large Eddy Simulations of thermal boundary layer developments in a turbulent channel flow under asymmetrical heating. *Computers & Fluids*, 151: 159–176, June 2017.
- R. Buck and S. Giuliano. Solar tower system temperature range optimization for reduced LCOE. *AIP Conference Proceedings*, 2126(1):030010, July 2019.
- C. Calvin, O. Cueto, and P. Emonot. An object-oriented approach to the design of fluid mechanics software. *ESAIM: Mathematical Modelling and Numerical Analysis - Modélisation Mathématique et Analyse Numérique*, 36(5):907–921, 2002.
- J. Capeillère, A. Toutant, G. Olalde, and A. Boubault. Thermo-mechanical behavior of a plate ceramic solar receiver irradiated by concentrated sunlight. *Solar Energy*, 110:174–187, Nov. 2014.
- X. Daguene-Frick, J.-M. Foucaut, S. Coudert, A. Toutant, and G. Olalde. Experimental Analysis of the Turbulent Flow Behavior of a Textured Surface Proposed for Asymmetric Heat Exchangers. *Flow, Turbulence and Combustion*, 89(1):149–169, July 2012.
- M. David, A. Toutant, and F. Bataille. Direct simulations and subgrid modeling of turbulent channel flows asymmetrically heated from both walls. *Physics of Fluids*, 33(8):085111, Aug. 2021.
- M. David, A. Toutant, and F. Bataille. Investigation of thermal large-eddy simulation approaches in a highly turbulent channel flow submitted to strong asymmetric heating. *Physics of Fluids*, 33(4):045104, Apr. 2021.
- M. David, A. Toutant, and F. Bataille. Numerical development of heat transfer correlation in asymmetrically heated turbulent channel flow. *International Journal of Heat and Mass Transfer*, 164:120599, Jan. 2021.
- R. B. Dean. Reynolds Number Dependence of Skin Friction and Other Bulk Flow Variables in Two-Dimensional Rectangular Duct Flow. *Journal of Fluids Engineering*, 100(2):215–223, June 1978.
- S. Dong, F. Tong, M. Yu, J. Chen, X. Yuan, and Q. Wang. Effects of wall temperature on two-point statistics of the fluctuating wall shear stress and heat flux in supersonic turbulent boundary layers. *Physics of Fluids*, 34(6):065114, June 2022.
- V. Driest. On Turbulent Flow Near a Wall. *Journal of the Aeronautical Sciences*, 23(11):1007–1011, 1956.
- D. Dupuy, A. Toutant, and F. Bataille. Turbulence kinetic energy exchanges in flows with highly variable fluid properties. *Journal of Fluid Mechanics*, 834:5–54, Jan. 2018.
- S. Hoyas and J. Jiménez. Reynolds number effects on the Reynolds-stress budgets in turbulent channels. *Physics of Fluids*, 20(10):101511, Oct. 2008.
- N. Hutchins and I. Marusic. Evidence of very long meandering features in the logarithmic region of turbulent boundary layers. *Journal of Fluid Mechanics*, 579:1–28, May 2007.
- N. Hutchins and I. Marusic. Large-scale influences in near-wall turbulence. *Philosophical Transactions of the Royal Society A: Mathematical, Physical and Engineering Sciences*, 365(1852): 647–664, Mar. 2007.
- N. Kasagi, Y. Tomita, and A. Kuroda. Direct Numerical Simulation of Passive Scalar Field in a Turbulent Channel Flow. *Journal of Heat Transfer*, 114(3):598–606, Aug. 1992.
- H. Kawamura, K. Ohsaka, H. Abe, and K. Yamamoto. DNS of turbulent heat transfer in channel flow with low to medium-high Prandtl number fluid. *International Journal of Heat and Fluid Flow*, 19(5):482–491, Oct. 1998.
- H. Kawamura, H. Abe, and Y. Matsuo. DNS of turbulent heat transfer in channel flow with respect to Reynolds and Prandtl number effects. *International Journal of Heat and Fluid Flow*, 20(3):196–207, June 1999.
- W. M. Kays. Turbulent Prandtl Number—Where Are We? *Journal of Heat Transfer*, 116(2):284–295, May 1994.

- J. Kim and P. Moin. Transport of Passive Scalars in a Turbulent Channel Flow. In J.-C. André, J. Cousteix, F. Durst, B. E. Launder, F. W. Schmidt, and J. H. Whitelaw, editors, *Turbulent Shear Flows 6*, pages 85–96, Berlin, Heidelberg, 1989. Springer. ISBN 978-3-642-73948-4.
- J. Kim, P. Moin, and R. Moser. Turbulence statistics in fully developed channel flow at low Reynolds number. *Journal of Fluid Mechanics*, 177:133–166, Apr. 1987.
- M. Kozuka, Y. Seki, and H. Kawamura. DNS of turbulent heat transfer in a channel flow with a high spatial resolution. *International Journal of Heat and Fluid Flow*, 30(3):514–524, June 2009.
- A. Kribus, P. Doron, R. Rubin, J. Karni, R. Reuven, S. Duchan, and E. Taragan. A Multistage Solar Receiver: The Route To High Temperature. *Solar Energy*, 67(1):3–11, July 1999.
- A. V. Kuznetsov and D. A. Nield. Forced convection in a channel partly occupied by a bidisperse porous medium: Asymmetric case. *International Journal of Heat and Mass Transfer*, 53(23):5167–5175, Nov. 2010.
- S. L. Lyons, T. J. Hanratty, and J. B. McLaughlin. Direct numerical simulation of passive heat transfer in a turbulent channel flow. *International Journal of Heat and Mass Transfer*, 34(4):1149–1161, Apr. 1991.
- R. P. Merchán, M. J. Santos, A. Medina, and A. Calvo Hernández. High temperature central tower plants for concentrated solar power: 2021 overview. *Renewable and Sustainable Energy Reviews*, 155:111828, Mar. 2022.
- R. D. Moser, J. Kim, and N. N. Mansour. Direct numerical simulation of turbulent channel flow up to  $Re\tau=590$ . *Physics of Fluids*, 11(4):943–945, Jan. 1999.
- Y. Na, D. V. Papavassiliou, and T. J. Hanratty. Use of direct numerical simulation to study the effect of Prandtl number on temperature fields. *International Journal of Heat and Fluid Flow*, 20(3):187–195, June 1999.
- F. Nicoud. Conservative High-Order Finite-Difference Schemes for Low-Mach Number Flows. *Journal of Computational Physics*, 158(1):71–97, Feb. 2000.
- F. Nicoud and P. Bradshaw. A velocity transformation for heat and mass transfer. *Physics of Fluids*, 12(1):237–238, Jan. 2000.
- P. Orlandi, D. Sassun, and S. Leonardi. DNS of conjugate heat transfer in presence of rough surfaces. *International Journal of Heat and Mass Transfer*, 100:250–266, Sept. 2016.
- S. Paolucci. Filtering of sound from the Navier-Stokes equations. *NASA STI/Recon Technical Report N*, 83, 1982.
- A. Patel, J. W. R. Peeters, B. J. Boersma, and R. Pecnik. Semi-local scaling and turbulence modulation in variable property turbulent channel flows. *Physics of Fluids*, 27(9):095101, Sept. 2015.
- S. Rittidech and S. Wannapakne. Experimental study of the performance of a solar collector by closed-end oscillating heat pipe (CEOHP). *Applied Thermal Engineering - APPL THERM ENG*, 27:1978–1985, Aug. 2007.
- R. L. Simpson. Characteristics of turbulent boundary layers at low Reynolds numbers with and without transpiration. *Journal of Fluid Mechanics*, 42(4):769–802, 1970.
- W. Sutherland. The viscosity of gases and molecular force. *The London, Edinburgh, and Dublin Philosophical Magazine and Journal of Science*, 36(223):507–531, Dec. 1893.
- A. Toutant and F. Bataille. Turbulence statistics in a fully developed channel flow submitted to a high temperature gradient. *International Journal of Thermal Sciences*, 74:104–118, Dec. 2013.
- A. Trettel and J. Larsson. Mean velocity scaling for compressible wall turbulence with heat transfer. *Physics of Fluids*, 28(2):026102, Feb. 2016.
- M. Zheng, J. Zapata, C.-A. Asselineau, J. Coventry, and J. Pye. Analysis of tubular receivers for concentrating solar tower systems with a range of working fluids, in exergy-optimised flow-path configurations. *Solar Energy*, 211:999–1016, Nov. 2020.